Monthly Notices of the ROYAL ASTRONOMICAL SOCIETY

MNRAS **540,** 1909–1927 (2025) https://doi.org/10.1093/mnras/staf684
Advance Access publication 2025 May 1

TOI-6478 b: a cold underdense Neptune transiting a fully convective M dwarf from the thick disc

Madison G. Scott [1★] Amaury H.M.J. Triaud [1] Khalid Barkaoui [2,3,4] Daniel Sebastian [1] Adam J. Burgasser [5] Karen A. Collins [6] Georgina Dransfield [1,7,8] Coel Hellier [9] Steve B. Howell [10] Anjali A. A. Piette [1] Benjamin V. Rackham [3] Keivan G. Stassun [11] Amalie Stokholm [1] Mathilde Timmermans [1,2] Cristilyn N. Watkins [6] Michael Fausnaugh [12] Akihiko Fukui [3,13] Jon M. Jenkins [10] Norio Narita [4,13,14] George Ricker [15] Emma Softich [5] Richard P. Schwarz [6] Sara Seager [15,16,17] Avi Shporer [18] Christopher Theissen [5] Joseph D. Twicken [10,19] Joshua N. Winn[20] and David Watanabe [21]

Affiliations are listed at the end of the paper

Accepted 2025 April 9. Received 2025 April 9; in original form 2025 January 13

ABSTRACT

Growing numbers of exoplanet detections continue to reveal the diverse nature of planetary systems. Planet formation around late-type M dwarfs is of particular interest. These systems provide practical laboratories to measure exoplanet occurrence rates for M dwarfs, thus testing how the outcomes of planet formation scale with host mass, and how they compare to Sun-like stars. Here, we report the discovery of TOI-6478 b, a cold ($T_{\rm eq} = 204$ K) Neptune-like planet orbiting an M5 star ($R_\star = 0.234 \pm 0.012\,{\rm R}_\odot$, $M_\star = 0.230 \pm 0.007\,{\rm M}_\odot$, $T_{\rm eff} = 3230 \pm 75$ K) that is a member of the Milky Way's thick disc. We measure a planet radius of $R_b = 4.6 \pm 0.24\,{\rm R}_\oplus$ on a $P_b = 34.005019 \pm 0.000025$ d orbit. Using radial velocities, we calculate an upper mass limit of $M_b \leq 9.9\,{\rm M}_\oplus$ ($M_b \leq 0.6\,{\rm M}_{\rm Nep}$), with $3\,\sigma$ confidence. TOI-6478 b is a milestone planet in the study of cold Neptune-like worlds. Due to its large atmospheric scale height, it is amenable to atmospheric characterization with facilities such as *JWST*, and will provide an excellent probe of atmospheric chemistry in this cold regime. It is one of very few transiting exoplanets that orbit beyond their system's ice-line whose atmospheric chemical composition can be measured. Based on our current understanding of this planet, we estimate TOI-6478 b's spectroscopic features (in transmission) can be $\sim 2.5\times$ as high as the widely studied planet K2-18 b.

Key words: planets and satellites: detection – planets and satellites: fundamental parameters – planets and satellites: gaseous planets – stars: low-mass.

1 INTRODUCTION

Over 75 per cent of stars in our Galaxy are classified as M dwarfs (Chabrier 2003; Henry et al. 2006; Reylé et al. 2021). Their slow evolution, complex spectra, and low luminosities make accurate stellar characterization tricky compared to solar-type stars; however, efforts by studies such as the EBLM project (Eclipsing Binaries–Low Mass; Triaud et al. 2013; Maxted, Triaud & Martin 2023) aim to populate the mass–radius parameter for these stars. More specifically, they investigate the low-mass end of this parameter space, i.e. fully convective M dwarfs ($\leq 0.35\,{\rm M}_\odot$; Torres, Andersen & Giménez 2010; Moya et al. 2018), where stellar evolution models likely underestimate stellar radii (see e.g. Casagrande, Flynn & Bessell 2008; Spada et al. 2013; Kesseli et al. 2018; Duck et al. 2023; Davis et al. 2024; Swayne et al. 2024). Improving mass–radius relations for low-mass stars is crucial because planets discovered transiting these stars provide astronomers with a particularly good opportunity to make detailed atmospheric characterizations, for instance, with the *JWST* (The JWST Transiting Exoplanet Community Early Release Science Team et al. 2022) (see e.g. Benneke et al. 2019; Madhusudhan et al. 2020; Kempton et al. 2023). Planets transiting M dwarfs produce comparatively larger transit depths than similar planets transiting Sun-like stars. Similarly, transmission spectroscopy is a modulation of the transit depth by the transiting planet's (TP) atmosphere, and this modulation is also larger when the star is smaller, for a fixed planet size. Smaller stellar radii makes it also easier to perform follow-up observations using ground-based facilities (e.g. Brown et al. 2013; Sebastian et al. 2021; Triaud 2021).

To date, the *Transiting Exoplanet Survey Satellite* (*TESS*; Ricker et al. 2015) has identified over 7000 exoplanet candidates. Of the 600 confirmed,[1] there are less than 30 Neptune-sized planets that orbit M dwarfs, and less that 10 orbiting late-type M dwarfs ($T_{\rm eff} \leq 3300$ K).

★ E-mail: mgs947@student.bham.ac.uk

[1]NASA Exoplanet Archive, 2025 January https://exoplanetarchive.ipac.caltech.edu/

These planets present a unique opportunity to probe Neptune-like planet formation around stars much different to the Sun.

TOI-6478 b is a cold, seemingly underdense ($\leq 0.56\,\mathrm{g\,cm^{-3}}$), Neptune-sized planet orbiting a cool late-type fully convective M dwarf. Similar to exoplanets such as TOI-620 b (Reefe et al. 2022), this exoplanet appears to be of low density, indicative of a high atmospheric mass fraction.

A sub-category of these low-density exoplanets, namely 'super-puffs', is defined to be those that have densities $\leq 0.3\,\mathrm{g\,cm^{-3}}$ (e.g. Cochran et al. 2011; Santerne et al. 2019). It has been speculated that some superpuff planets could be explained as ringed exoplanets (Piro & Vissapragada 2020) or planets with hazy atmospheres (Gao & Zhang 2020), which can explain their apparent inflated radii.

Underdense exoplanets provide an exciting opportunity for observations with *JWST* because their large atmospheric scale heights enhance the detection of transmission spectroscopy features. While this is desirable for all kinds of exoplanets, it is especially compelling for planets that lie in the poorly populated region of parameter space of cold (< 250 K), short-period (< 50 d) planets. More specifically, Neptune-sized planets within this temperature range likely have cool H_2/He-dominated atmospheres, more akin to the giant planets of our Solar system than most exoplanets discovered thus far (e.g. Nettelmann et al. 2010; Seager & Deming 2010). They therefore represent an important link between the exoplanet population and the planets in our Solar system. Cool atmospheres of planets beyond the ice-line are relatively understudied because most orbit Sun-like stars and consequently have long orbital periods (> 100 d), making transmission spectroscopy challenging and impractical. Our paper highlights the remarkable opportunity that TOI-6478 b presents for atmospheric and planet formation studies.

Another interesting property of the TOI-6478 system is in being part of the thick disc, which implies an age older than the Solar system. A recent population study reveals hints that underdense planets appear more likely in older systems (Weeks et al. 2025), a trend TOI-6478 b appears to follow.

This paper is organized as follows. In Section 2, we describe the observations and methods used to characterize the host star. Section 3 describes the conclusions we are able to draw from the available *TESS* data, and Section 4 presents the photometric and radial-velocity ground-based follow-up observations used for the validation of TOI-6478 b's planetary nature. Section 5 describes the joint photometric and radial-velocity fitting, followed by a discussion and conclusion of these results in Section 6.

2 STELLAR CHARACTERIZATION

TOI-6478 is a nearby (38 pc; Bailer-Jones et al. 2021) M dwarf of spectral type M5, with an M3 co-moving companion. The planetary information will be derived using the host star's parameters, therefore we describe the characterization of TOI-6478 in the following sections. All photometry and stellar parameters adopted for this work can be found in Table 1.

Table 1. Stellar parameters adopted for this work.

Designations	TOI-6478, TIC 332657786, 2MASS J09595797-1609323, *Gaia* DR2 5673934548598976256, UCAC4 370–057370, WISE J095958.01-160934.4, LP 789–76B	
Parameter	**Value**	**Source**
T mag	13.0041±0.0082	Stassun et al. (2019)
V mag	15.99±0.2	Stassun et al. (2019)
G mag	14.313±0.00069	Gaia Collaboration (2022)
J mag	11.389±0.024	Cutri et al. (2003)
H mag	10.91±0.022	Cutri et al. (2003)
K mag	10.657±0.021	Cutri et al. (2003)
W1 mag	10.488±0.022	Cutri et al. (2021)
W2 mag	10.261±0.021	Cutri et al. (2021)
W3 mag	10.14 ±0.061	Cutri et al. (2021)
W4 mag	9.105 ±0.525	Cutri et al. (2021)
Distance	38.61±0.1 pc	Stassun et al. (2019)
α	09:59:58.03	Gaia Collaboration (2022)
δ	-16:09:35.26	Gaia Collaboration (2022)
μ_α	52.4 mas yr^{-1}	Gaia Collaboration (2022)
μ_δ	-172.3 mas yr^{-1}	Gaia Collaboration (2022)
SpT (optical)	M5	This work
SpT (NIR)	M4.0±0.5	This work
$R_\star$	0.234±0.012 $R_\odot$	This work
$M_\star$	0.230± 0.007 $M_\odot$	This work
$T_{\rm eff}$	3230±75 K	This work
	3193±1 K	Gaia Collaboration (2022)
log $g_\star$	5.016±0.005	Gaia Collaboration (2022)
[Fe/H]	−0.18±0.20 dex	This work (opt. spectroscopy)
[Fe/H]	−0.53±0.13 dex	This work (NIR spectroscopy)
	−0.195±0.003 dex	Gaia Collaboration (2022)
Age	$\gtrsim$6–7 Gyr	This work (spectroscopy)

2.1 Reconnaissance spectroscopy

2.1.1 Shane/Kast

TOI-6478 and its brighter co-moving companion LP 789-76 A (aka 2MASS J09595660−1609206, aka TIC 332657787, aka *Gaia* DR3 5673934617318453248; $G = 12.68$, 23 arcsec separation) were observed simultaneously with the Shane 3m Kast double spectrograph (Miller & Stone 1994) on 2024 April 9 (UT). Conditions were clear and windy with 1 arcsec seeing, and we used the 1.5 arcsec (3.5 pixel) slit rotated to include both sources. We used the 600/4310 grism on the blue channel to acquire 3750–5600 Å spectra at a resolution of $\lambda/\Delta\lambda \approx 1200$, and the 600/7500 grating on the red channel to acquire 5800–9000 Å spectra at a resolution of $\lambda/\Delta\lambda \approx 1500$. Total integrations of 1000 s were acquired in both channels, split into two exposures of 500 s each in the red, at an average airmass of 1.70. We observed the nearby G2 V star 43 Hya ($V = 7.62$) immediately afterwards at a similar airmass for telluric absorption correction, and the flux standard Feige 34 ($V = 11.2$; Massey & Gronwall 1990; Oke 1990) later in the night. Arclamps (HeHgCd in the blue, HeNeAr in the red), quartz flat field lamps, and bias frames were obtained at the start of the night for wavelength and pixel response calibration.

Data were reduced using the `kastredux` package,[2] following standard approaches for optical spectroscopic data reduction. In brief, we used the flat field lamp exposures to trace the illuminated orders and measure pixel response, the lamp exposures and bias frames to define a mask array, and the arc lamps to determine the wavelength scale with a precision of 0.19 Å (13 km s^{-1}) in the blue and 0.23 Å (10 km s^{-1}) in the red. Source spectra were traced along the tilted dispersion axes and extracted using a boxcar profile with a linear fit to the background. The red data were also corrected for cosmic ray contamination using an outlier rejection algorithm between the two exposures. Spectral flux density calibration was determined from band measurements of Feige 34 from Massey & Gronwall (1990), with a second-order correction made using the G2 V telluric calibrator and an empirical template from Pickles (1998). The G2 V

[2] https://github.com/aburgasser/kastredux

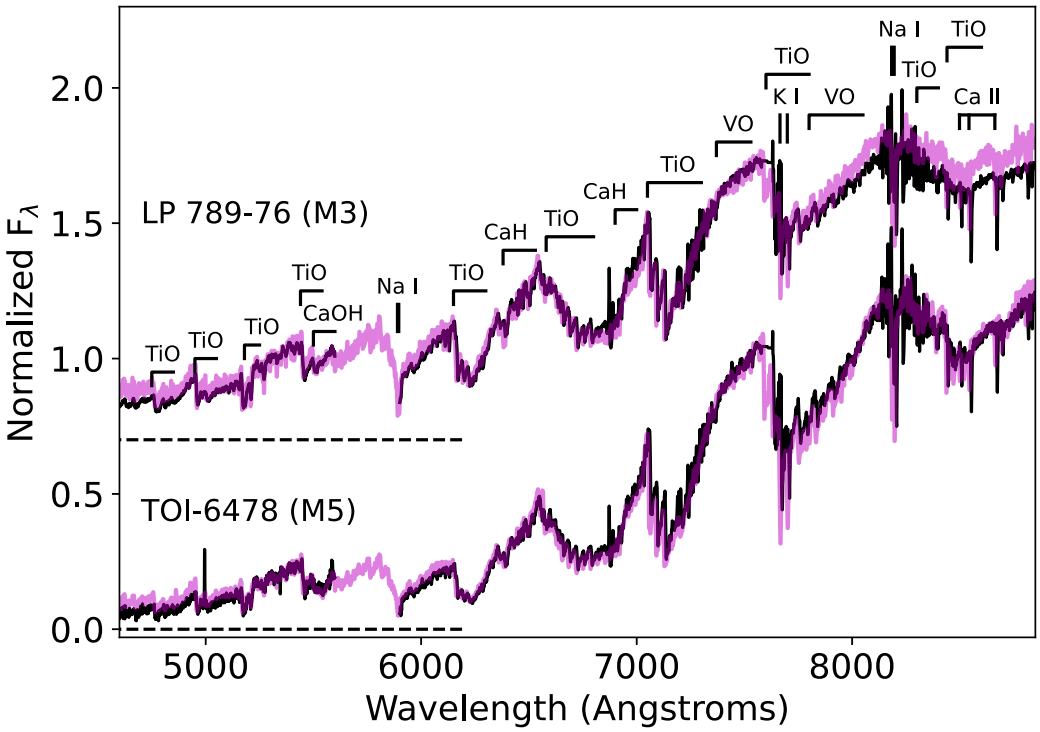

Figure 1. Kast spectra (black lines) of the co-moving companions LP 789-76 (top) and TOI-6478 (bottom) compared to the best-fitting M3 and M5 spectral templates from Bochanski et al. (2007; magenta lines). All spectra are normalized at 7500 Å, with the blue and red orders of Kast relatively scaled to match the spectral standard, and the spectrum of LP 789-76 is offset by 0.7 flux units for clarity (zero-points are indicated by dashed lines). Key atomic and molecular spectral features are labelled.

spectrum was also used to correct for telluric absorption in the science targets. Our final data, shown in Fig. 1, have signal-to-noise (S/N) of 22 at 5400 Å and 121 at 7500 Å for TOI-6478 and 96 at 5400 Å and 281 at 7500 Å for LP 789-76.

We used tools in `kastredux` to characterize both spectra, which display the characteristic molecular bands and red optical slope of early-to-mid M dwarfs. Comparison to SDSS spectral templates from Bochanski et al. (2007) yields classifications of M5 for TOI 6478 and M3 for LP 789-76, which are consistent with index-based classifications based on the system of Lépine, Rich & Shara (2003). We see no evidence of Hα or Hβ emission indicative of magnetic activity in either source. Indeed, TOI 6478 shows Hα in absorption with an equivalent width EW = 0.37±0.07 Å, suggesting a system activity age $\gtrsim$6–7 Gyr (West et al. 2008; Rebassa-Mansergas et al. 2023). Such an old age is consistent with the kinematics of the system. The Gaia Catalogue of Nearby Stars (Gaia Collaboration 2021) reports [U, V, W] = [+2,−99, +36] for LP 789-76, giving the system a 99 per cent probability of being part of the Galactic thick disc based on the results of Bensby, Feltzing & Lundström (2003).

Analysis of the metallicity-sensitive features of TiO and CaH around 6800–7100 Å yields discrepant ζ values of 0.85±0.01 and 1.01±0.01 for TOI 6478 and LP 789-76, respectively (Lépine et al. 2013). The former is close to the dwarf/subdwarf boundary defined by Lépine, Rich & Shara (2007), suggesting that the system may be slightly metal-poor, with an estimate of [Fe/H] = −0.18±0.20 based on Mann et al. (2013). The latter is consistent with solar metallicity. Both sources have atmosphere parameters reported in *Gaia* DR3, with metallicities that are consistent with our measurements and also discrepant with each other: [Fe/H] = −0.195±0.003 for TOI 6478 and −0.026±0.011 for LP 789-76. *Gaia* also reports effective temperatures of $T_{\rm eff}$ = 3193 and 3428 K (with unrealistic precisions of 1 K), respectively. The latter is consistent with the $T_{\rm eff}$ = 3456±115 K estimate of Hardegree-Ullman et al. (2023) using *Gaia* photometry and the empirical relationship of Pecaut & Mamajek (2013).

2.1.2 *IRTF/SpeX*

We gathered medium-resolution near-infrared spectra of TOI-6478 and its comoving companion LP 789–76 on 2024 May 10 (UT) using the SpeX spectrograph (Rayner et al. 2003) on the 3.2-m NASA Infrared Telescope Facility (IRTF). Conditions were clear, and seeing was 0.7 arcsec. We used the short-wavelength cross-dispersed (SXD) mode with the 0.3 arcsec × 15 arcsec slit aligned to the parallactic angle. This set-up provides 0.80–2.42 μm spectra at a resolving power of R∼2000 with 2.5 pixels per resolution element. While nodding in an ABBA pattern, we collected six 300-s integrations on TOI-6478 and six 120-s integrations on LP 789–76. We gathered a set of standard SXD flat-field and arc-lamp calibrations after each target, followed by six 20-s integrations of the A0 V standard HD 86593. We reduced the data with Spextool v4.1 (Cushing, Vacca & Rayner 2004), following the approach of previous analyses (Delrez et al. 2022; Barkaoui et al. 2023; Ghachoui et al. 2023). The final spectra of TOI-6478 and LP 789–76 have median per-pixel S/N of 111 and 141, respectively.

The SpeX SXD spectra of TOI-6478 and LP 789–76 are shown in Fig. 2. As in previous SpeX analyses (e.g. Triaud et al. 2023; Gillon et al. 2024; Timmermans et al. 2024), we used the SpeX Prism Library Analysis Toolkit (Burgasser & Splat Development Team 2017) to assign spectral types and estimate stellar metallicities. Comparing the spectra to standard spectra of single stars in the IRTF Spectral Library (Cushing, Rayner & Vacca 2005; Rayner, Cushing &

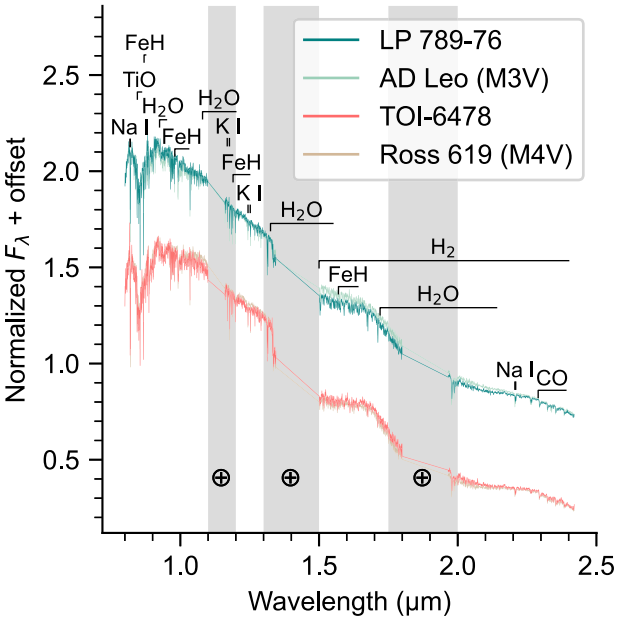

Figure 2. SpeX SXD spectra of TOI-6478 (coral) and LP 789–76 (teal) alongside their best-matching spectral standards. Prominent atomic and molecular spectral features of M dwarfs are highlighted.

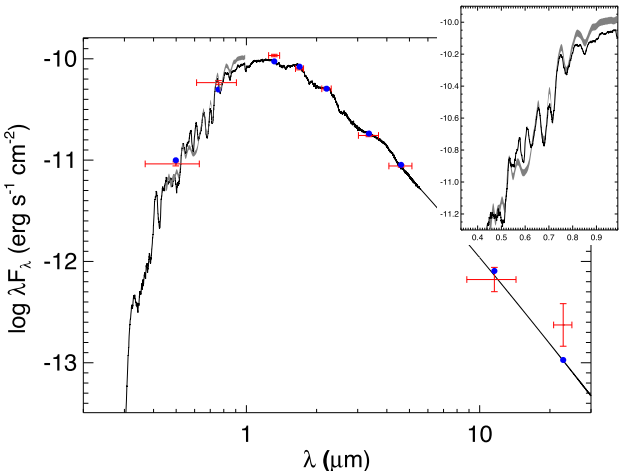

Figure 3. SED of TOI-6478. The red symbols represent the observed photometric measurements, where the horizontal bars represent the effective width of the passband. The blue symbols are the model fluxes from the best-fitting PHOENIX atmosphere model (black). The *Gaia* absolute flux-calibrated spectrophotometry is overlaid as the grey swathe (also shown in detail in the inset plot).

Vacca 2009), we find close matches to Ross 619 (M4V) and AD Leo (M3V) for TOI-6478 and LP 789–76, respectively. We therefore adopt infrared spectral types of M4.0 ± 0.5 for TOI-6478 and M3.0 ± 0.5 for LP 789–76. These are slightly earlier than and consistent with our optical spectral types, respectively. Using the H2O–K2 index (Rojas-Ayala et al. 2012) and Mann et al. (2013) relation, we estimate stellar iron abundances of [Fe/H] = −0.53 ± 0.13 for TOI-6478 and [Fe/H] = −0.48 ± 0.12 for LP 789–76, indicating a consistent sub-solar metallicity for both stars. For TOI-6478, this estimate is lower than our estimate based on the optical spectra but consistent with it at 1.5σ.

2.2 Spectral energy distribution

As an independent determination of the basic stellar parameters, we performed an analysis of the broad-band spectral energy distribution (SED) of the star together with the *Gaia* DR3 parallax (with no systematic offset applied; see e.g. Stassun & Torres 2021), in order to determine an empirical measurement of the stellar radius, following the procedures described in Stassun & Torres (2016), Stassun, Collins & Gaudi (2017), and Stassun et al. (2018). We pulled the the JHK_S magnitudes from *2MASS*, the W1–W4 magnitudes from *WISE*, the $G_{BP}G_{RP}$ magnitudes from *Gaia*, and the *Gaia* spectrophotometry. Together, the available photometry spans the full stellar SED over the wavelength range 0.4–20 μm (see Fig. 3).

We performed a fit using PHOENIX stellar atmosphere models (Husser et al. 2013a), fitting for the effective temperature ($T_{\rm eff}$) while adopting the metallicity ([Fe/H]) from the spectroscopic analysis. We fixed the extinction $A_V \equiv 0$ due to the close proximity of the system. The resulting fit (Fig. 3) has a best fit $T_{\rm eff} = 3230 \pm 75$ K, with a reduced χ^2 of 3.4 and consistent with the *Gaia* estimate. Integrating the model SED gives the bolometric flux at Earth, $F_{\rm bol} = 1.151 \pm 0.040 \times 10^{-10}$ erg s^{-1} cm^{-2}. Taking the $F_{\rm bol}$ and the *Gaia* parallax directly gives the bolometric luminosity, $L_{\rm bol} = 0.00534 \pm 0.00019$ L$_\odot$. The stellar radius then follows from the Stefan–Boltzmann relation, $R_\star = 0.234 \pm 0.012$ R$_\odot$. In addition, we can estimate the stellar mass from the empirical M_K relations of Mann et al. (2016), giving $M_\star = 0.230 \pm 0.007$ M$_\odot$. These values are consistent with $T_{\rm eff}$, $L_{\rm bol}$, and $R_\star$ estimates from Hardegree-Ullman et al. (2023) based on *Gaia* data alone, while our mass is nearly 3σ higher than the 0.203±0.006 M$_\odot$ reported in that study.

2.3 Galactic orbit of TOI-6478

The orbit of TOI-6478 in the Milky Way galaxy was computed from the 5D astrometric information and line-of-sight velocity from *Gaia* DR3 (Gaia Collaboration 2016, 2023). We use the PYTHON package `galpy` (Bovy 2015) for this computation of the Galactic orbital properties. As a description of the Milky Way potential, we use the axisymmetric gravitational potential `McMillan2017` (McMillan 2017). As for the Galactic location and velocity of the Sun, we assume $(X_\odot, Y_\odot, Z_\odot) = (8.2, 0, 0.0208)$ kpc and $(U_\odot, V_\odot, W_\odot) = (11.1, 12.24, 7.25)$ kms^{-1} with a circular velocity of 240 kms^{-1} (Schönrich, Binney & Dehnen 2010; Bovy 2015; Bennett & Bovy 2019; Gravity Collaboration 2019).

Fig. 4 shows the integration of the orbit of TOI-6478 in the Milky Way potential in Cartesian Galactocentric coordinates across a period of time of 5 Gyr, highlighting the extent of the system's movement within the Milky Way.

It is interesting to note that this system spends time both in the denser inner part of the Galactic disc, at a minimum inner distance about a factor of 2 closer to the Galactic centre than the solar orbit, and significantly further away from the Galactic mid-plane than our Sun, reaching a maximum height of almost 1 kpc over the course of its orbit.

Fig. 5 shows location of TOI-6478 in a so-called Toomre diagram. The diagram plots a star's velocity relative to the Sun in two components: along the horizontal axis it shows the component of a star's rotational velocity around in the plane of the Galaxy, and the vertical axis shows the combination of a star's velocity components perpendicular to the Galactic plane. From this diagram, it is evident that different Galactic stellar populations such as the thin disc, thick disc, and halo show different characteristics, with stars in the Galactic thin disc – like our Sun – move similar to the Sun and

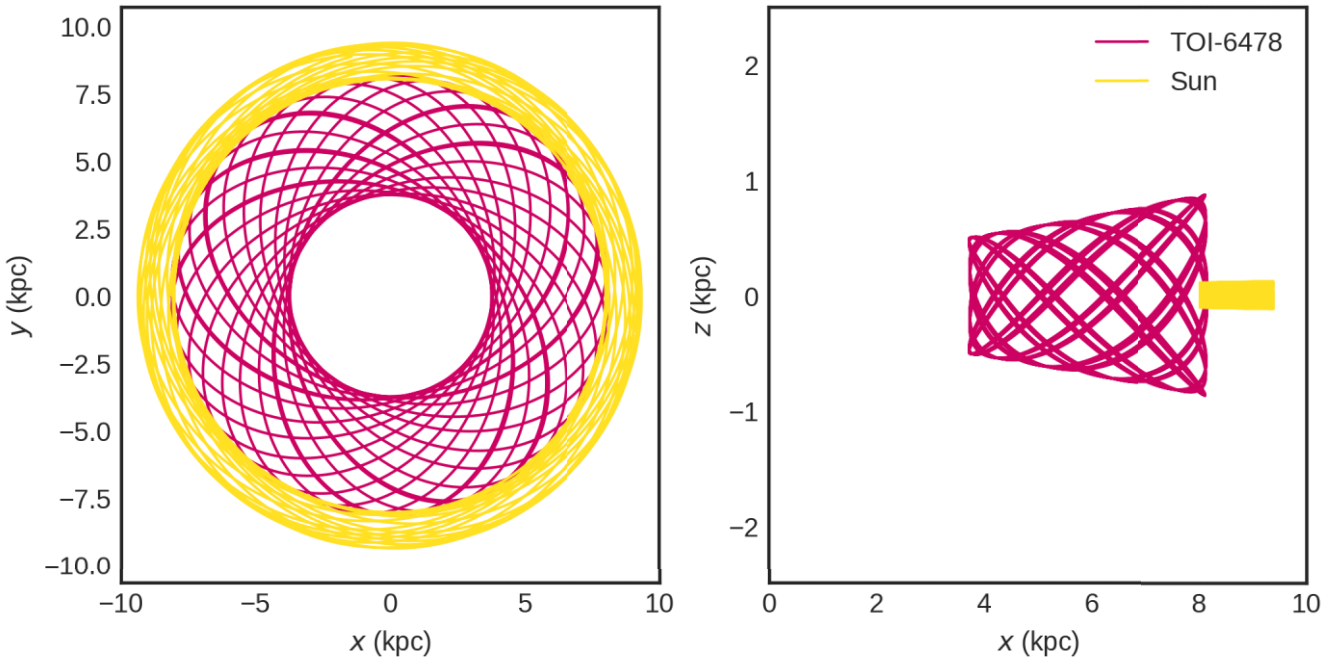

Figure 4. The integrated orbit of TOI-6478 within the Milky Way's potential over a 5 Gyr period, depicted in Cartesian Galactocentric coordinates. The left panel presents a top-down view (x, y), while the right panel shows an edge-on perspective (x, z). For comparison, the Sun's integrated orbit is included in both views.

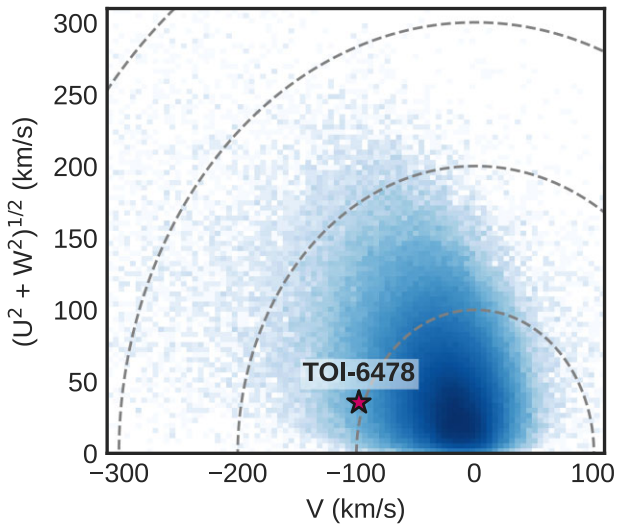

Figure 5. A Toomre diagram illustrating the Galactic velocity components perpendicular to the plane (vertical axis) versus those within the plane (horizontal axis). TOI-6478 is marked as a pink star. The background density map represents the number count of targets from *Gaia* DR3 identified as single stars with reliable astrometric data and available line-of-sight velocities (`astrometric_params_solved = 95`, `rv_nb_transits > 0`, `ruwe < 1.4`, and `non_single_star = 0`). The darker regions indicate higher target densities, prominently highlighting the Galactic thin disc around (0, 0).

thus the Galactic standard of rest ((0, 0) in Fig. 5) and with stars belonging to the Galactic halo rotating significantly slower than the Sun ($\gtrsim 200\,\mathrm{km s^{-1}}$) but move with higher velocities in the dimensions perpendicular to the Galactic plane.

TOI-6478 is found to be in the region of velocity and orbital space typically occupied by the Galactic thick disc stars. This identification is in alignment with the sub-solar metallicity (see Table 1), which is also characteristic for these stars. As the thick disc formed early on in the history of the Galaxy ($\gtrsim$ 9 Gyr Spitoni et al. 2024), this identification also agrees with the lower age bound estimated from the Hα lines.

The evolution of conditions for planet formation throughout the history of the Milky Way remains an area with many unresolved questions. Zink et al. (2023) conducted a demographic study of exoplanets around FGK dwarf stars and found that close-in small planets are approximately 50 per cent less common around stars in the Galactic thick disc compared to those in the thin disc, emphasizing how the Galactic surroundings affect the possible exoplanetary architecture. Hallatt & Lee (2025) attributed this difference to the more hostile conditions of the primordial thick disc, where the denser and more radiative environment likely led to the more efficient destruction of protoplanetary discs, thereby reducing the time-scale available for planet formation. TOI-6478 is an excellent candidate for future studies on the interior structure and atmospheric properties of planets in thick disc systems. These studies need to be extended to cover the abundant M dwarfs and with a greater sample we can explore variations in formation efficiency and evolutionary processes among planetary systems in different Galactic components.

3 *TESS* DATA

3.1 Determining the orbital period from *TESS* duo-transits

TESS observed two transits throughout three sectors (S8, S35, S62) with a cadence of 120 s. The data have been processed by the Science Processing Operations Centre (SPOC; Jenkins et al. 2016, Fig. 6). The signature of TOI-6478 b was detected first in a search of sectors 8, 35, and 62 by the FAINT search pipeline (Huang et al.

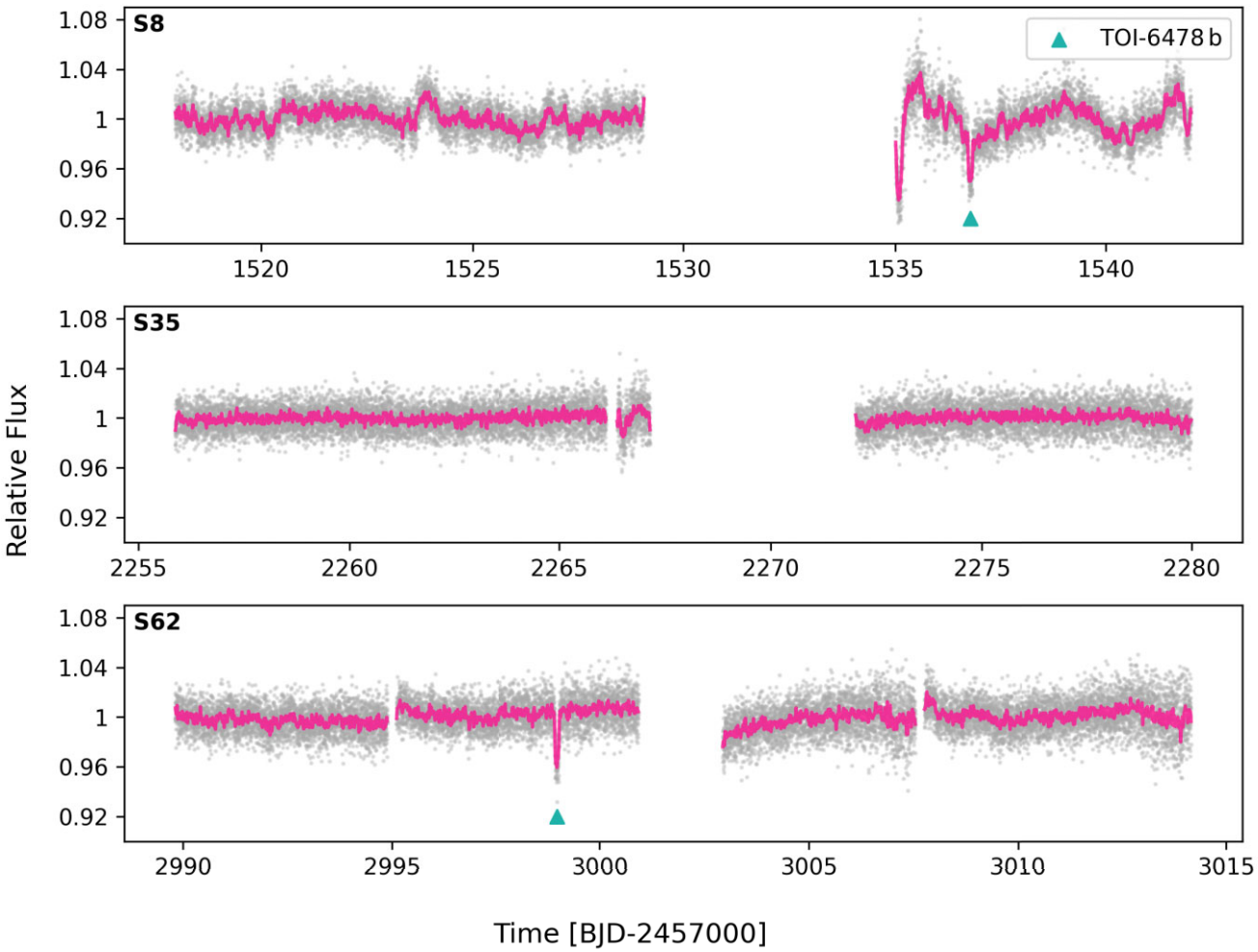

Figure 6. The SPOC PDCSAP *TESS* light curves for TOI-6478 b, observed at 120 s cadence. The star was observed in three sectors: sector 8, sector 35, and sector 62. The grey points show the 120 s data, and the pink points show these data binned to 20 mins. The transits detected in sector 8 and sector 62 are indicated by a green triangle.

2020a, b; Kunimoto & Daylan 2021) and was alerted by the TESS Science Office on 2023 June 15 (Guerrero et al. 2021a) after the data validation reports were vetted. The TESS SPOC detected the transit signature in the same sectors shortly thereafter with a noise-compensating matched filter (Jenkins 2002; Jenkins et al. 2010, 2020) and was fitted with an initial limb-darkened transit model (Li et al. 2019) and passed a suite of diagnostic tests (Twicken et al. 2018) including the difference image centroid test that located the host star within 3.0+/−2.5 arcsec of the transit source.

Prior to the QLP faint transit search detection, and subsequent alert as TOI-6478.01, the transit signature was flagged as a planet candidate CTOI by the Planet Hunters (Eisner et al. 2021) on 2020 May 15 based only on the first transit. TOI-6478.01 was then alerted by the TESS Science Office as a planet candidate on 2023 June 15, as discussed above.

Transit 1 occurred at 1536.7668 BTJD (S8) and transit 2 occurred 1462.21 d later in S62 at 2998.9728 BTJD. Based on the observed transit duration (∼3 h) and the available data (e.g. considering gaps where transits could fall), we predicted an orbital period of 34 d. Longer orbital periods that were compatible with the data were ruled out based on an incompatibility with the duration. We initiated a ground-based follow-up photometric observation (see Section 4.3.1), on 2024 March 3 assuming the approximate 34 d orbital period. A full transit was observed at a transit time of 3373.0354 BTJD, thus confirming this orbital period.

3.2 Aperture photometry

Fig. 7 shows the target pixel files (TPFs) for S8 and S62 for TOI-6478 b. Due to the large pixel size of *TESS* (21 arcsec px^{-1}), it is not uncommon to have crowding within the aperture. Here, we see that our target is blended in the *TESS* aperture with its brighter, co-moving companion LP 789–76 (23 arcsec separation). The flux contribution from this star can cause the transits we observe in *TESS* to be diluted in contrast to the transits we obtain from the ground (see Section 4.3.1), which typically have smaller apertures. The TPFs with the associated apertures are shown in Fig. 7. We also show the surrounding stars in the field (plot obtained from `triceratops`).

4 VETTING AND VALIDATION

This section describes the efforts taken to validate the planetary nature of TOI-6478 b. We first describe the high-resolution imaging observations, followed by an outline of the ground-based photometric

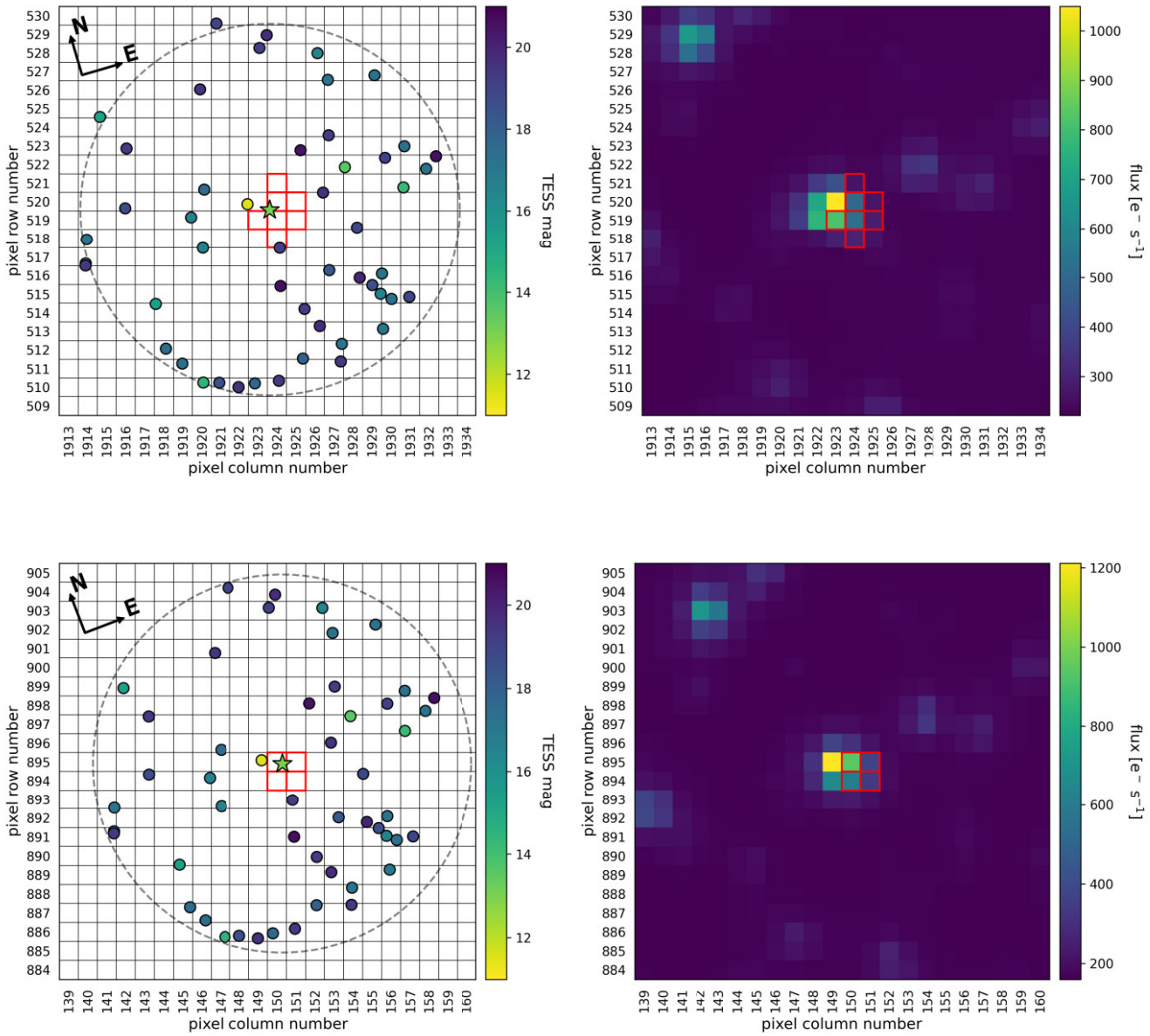

Figure 7. Left: stars within the field of the target star TOI-6478 (depicted by the star), obtained from the `triceratops` pipeline for sector 8 (top) and sector 62 (bottom). The colours of each star correspond to their *TESS magnitude*. The red shows the *TESS* pipeline aperture. The yellow point is the brighter comoving companion to TOI-6478, LP 789-76. Right: *TESS* TPFs with pipeline apertures for sector 8 (top) and sector 62 (bottom).

and radial velocity (RV) observations collected from the LCO and Gemini North observatories, respectively. We conclude this section with a discussion of how these observations were used in the validation of TOI-6478 b as a planetary candidate. All follow-up observations are summarized in Table 2.

4.1 Archival imaging

In order to investigate whether a background object is blending with the target star, we examine archival imaging of the field of view of TOI-6478. Given its high proper motion of 180 mas yr^{-1} (Gaia Collaboration 2022), this is able to be done through inspection of DSS/POSS-I and DSS/POSS-II (Reid et al. 1991; Lasker et al. 1996) images taken in red in 1953 and 1986, respectively, and comparing to the z_s-band MuSCAT4 (Narita et al. 2020) observations taken in 2024, 71 yr later (see Fig. 8). We can thus conclude that at TOI-6478's current position, there is no background star that could be impacting our conclusions due to being the source of the observed transit events.

4.2 High-resolution imaging

A critical observation to perform in order to rule out false positives such as background eclipsing binaries (EBs) is that of obtaining high-resolution images of the exoplanet host star. While nearby M stars such as TOI-6478 have proper motions that allow historic sky imagery to eliminate confounding stars at the present day position of the exoplanet host, the spatial scale of such images as well as present day seeing limited images cannot rule out stellar companions. Inside of 0.5 arcsec (19 au at the distance of TOI-6478), essentially no

Table 2. Summary of ground-based follow-up observations carried out for TOI-6478 b.

Follow-up observations				
High-resolution imaging				
Observatory	**Filter**	**Date**	**Sensitivity limit**	**Result**
Gemini South	562 nm	2024 Mar 13	$\Delta m = 4.84$ at $0.5''$	No sources detected
Gemini South	832 nm	2024 Mar 13	$\Delta m = 6.97$ at $0.5''$	No sources detected
Photometric follow-up				
Observatory	**Filter**	**Date**	**Coverage**	**Result**
LCO-SSO−2m0M	*Pan-STARRS-z_s*	2024 Mar 3	Full	Detection
LCO-SSO−2m0M	*Sloan-i'*	2024 Mar 3	Full	Detection
LCO-SSO−2m0M	*Sloan-r'*	2024 Mar 3	Full	Detection
LCO-SSO−2m0M	*Sloan-g'*	2024 Mar 3	Full	Detection
LCO-SSO−1m0	*Pan-STARRS-zs*	2024 Mar 3	Full	Detection
LCO-SSO−1m0	*V*	2024 Mar 3	Full	Detection
Spectroscopic observations				
Instrument	**Wavelength Range**	**Date**	**Number of Spectra**	**Use**
Shane/Kast	375–560 nm & 580–900 nm	2024 Apr 9	1	Stellar characterization
IRTF/SpeX	800–2420 nm	2024 May 10	1	Stellar characterization
Gemini North/MAROON-X	500–670 nm & 650–920 nm	2024 Mar 29–2024 Apr 23	10	Mass upper limit

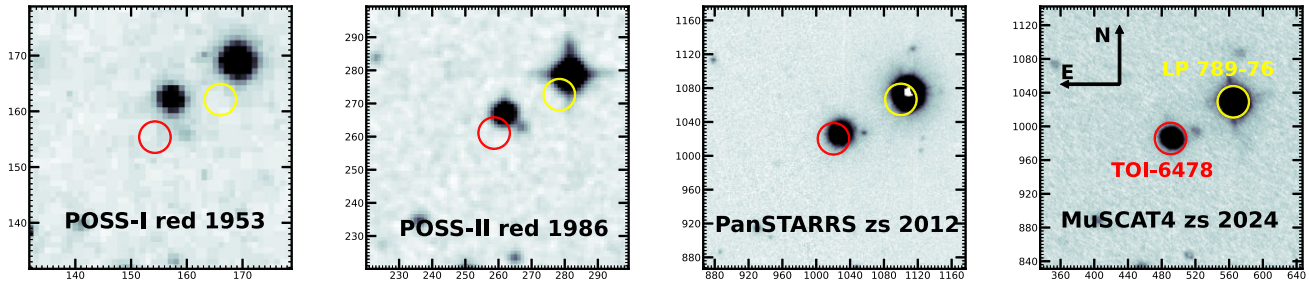

Figure 8. Archival images of the field of view around TOI-6478. From left to right: image taken with the DSS/POSS-I in 1953, image taken with the DSS/POSS-II in 1986 in red, image taken with PanSTARRS in 2012 in the z_s band, and the image taken with MuSCAT4 in 2024 in the z_s band. The red and yellow circles depict the positions of TOI-6478 and LP 789-76 in the 2024 image, respectively.

technique other than high-resolution imaging allows for search and detection of very close bound companions. Optical high-resolution speckle offers angular resolutions and deep contrast levels from which M star stellar companions can readily be identified. Spatially close bound companions produce 'third-light' flux that can lead to underestimated planetary radii if not accounted for in the transit model (Ciardi et al. 2015), incorrect planet and star parameters (Furlan & Howell 2017, 2020), and can cause non-detections of small planets residing with the same exoplanetary system (Lester et al. 2021). Thus, to search for very close bound companions, unresolved in *TESS* or other ground-based follow-up observations, we obtained high-resolution imaging speckle observations of TOI-6478.

TOI-6478 was observed on 2024 March 13 UT using the Zorro speckle instrument on the Gemini South 8-m telescope (Scott et al. 2021). Zorro provides simultaneous speckle imaging in two bands (562 and 832 nm) with output data products including a reconstructed image with robust contrast limits on companion detections (e.g. Howell et al. 2016). Due to the red nature of the M star TOI-6478, 16 sets of 1000 × 0.06 s images were obtained and processed in our standard reduction pipeline (Howell et al. 2011). Fig. 9 shows our final 5σ magnitude contrast curves and the 832 nm reconstructed speckle image. We find that, with the Zorro field of view, TOI-6478 is a single star with no companion brighter than 5–7.5 mag below that of the target star from the Gemini 8-m telescope diffraction limit (20 mas) out to 1.2 arcsec. At the distance of TOI-6478 ($d = 38$ pc) these angular limits correspond to spatial limits of 0.76 to 45 au. Another false positive scenario is that there is a bounded stellar companion below the Zorro detection sensitivity that is the source of the transit signal. This would mean that TOI-6478 has a wide binary companion that has a magnitude $\geq 7.5\times$ fainter and an angular separation up to around 1 arcsec. Using the Baraffe et al. (2015) models in I band (Zorro wavelength), assuming an old > 10 Gyr star (thick disc – see Section 2.3), the mass of a body $7.5\times$ fainter than TOI-6478 is $\sim 0.072\,M_\odot$, corresponding to a brown dwarf just below the hydrogen burning limit. This magnitude difference results in a flux ratio of $f_{\rm BD}/f_{\rm TOI-6478} = 0.001$. Therefore, if the transit event were to be on this brown dwarf companion, it would be diluted by 1000 due to the flux from TOI-6478, creating an unphysical transit depth (~ 0.004 per cent). The observed transit depth is already $\sim 40\times$ too deep compared to the largest eclipse that could happen on the possible bounded brown dwarf companion. We thus conclude that even if there is a bounded companion, the transit cannot be happening on this companion.

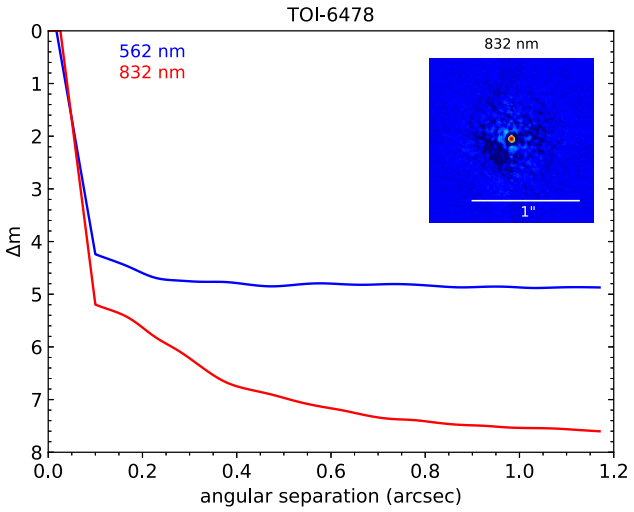

Figure 9. 5σ speckle imaging contrast curves obtained with Zorro for TOI-6478 in 562 and 832 nm bands on 2024 March 13, as a function of angular separation. The reconstructed 832 nm speckle image is shown in the top right inset with a 1 arcsec scale bar. No close companions are detected within the angular and brightness contrast levels.

4.3 Photometric follow-up

4.3.1 LCOGT photometry

The *TESS* pixel scale is ~ 21 arcsec pixel^{-1} and photometric apertures typically extend out to roughly 1 arcmin, generally causing multiple stars to blend in the *TESS* photometric aperture. To determine the true source of the *TESS* detection, we acquired ground-based time-series follow-up photometry of the field around TOI-6478 as part of the TESS Follow-up Observing Program (Collins 2019).[3] The on-target follow-up light curves are also used to place constraints on the transit depth and the *TESS* ephemeris. We used the TESS TRANSIT FINDER, which is a customized version of the TAPIR software package (Jensen 2013), to schedule our transit observations.

We observed a full transit of TOI-6478.01 on UTC 2024 March 3 simultaneously from 1.0 and 2.0 m telescopes at the Las Cumbres Observatory Global Telescope (LCOGT) (Brown et al. 2013) node at Siding Spring Observatory near Coonabarabran, Australia (SSO). Alternating Johnson/Cousins V and Pan-STARRS z_s filters were used from the 1 m network node, while simultaneous images were taken in Sloan g', r', i', and *Pan-STARRS*-z_s bands from the 2 m Faulkes Telescope South. The 1 m telescope is equipped with a 4096 × 4096 SINISTRO camera having an image scale of 0.389 arcsec per pixel, resulting in a 26 arcmin × 26 arcmin field of view. The 2 m telescope is equipped with the MuSCAT4 multiband imager (Narita et al. 2020). All images were calibrated by the standard LCOGT `BANZAI` pipeline (McCully et al. 2018), and differential photometric data were extracted using `AstroImageJ` (Collins et al. 2017). We used circular photometric apertures with radii in the range 2.4–4.7 arcsec, which excluded all of the flux from the nearest known neighbour in the *Gaia* DR3 catalogue (Gaia DR3 5673934617318453248, LP 789–76), which is 22.9 arc-sec north-east of TOI-6478. A ∼34 ppt event was detected on-target and confirms the 34 d period alias. All light-curve data are available on the `EXOFOP-TESS` website[4] and are included in the global modelling described in Section 5.

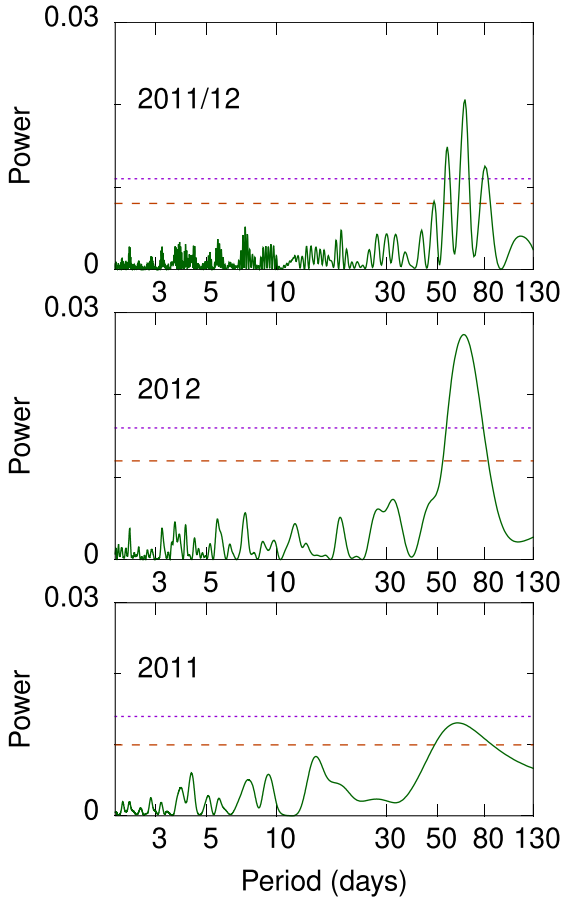

Figure 10. Periodograms of the WASP data for TOI-6478 and its co-moving companion from 2011 and 2012 and (top) both years combined. The dashed lines are at the estimated 10 per cent- and 1 per cent-likelihood false-alarm levels. There is a significant modulation at a period of 66 ± 4 d, though it is unclear which star it originates from.

4.3.2 WASP

The Wide Angle Search for Planets (WASP) project (Pollacco et al. 2006) was a ground-based exoplanet transit survey with instruments in La Palma and South Africa. In 2011 and 2012 it covered the field of TOI-6478. The resulting data indicate a possible rotational modulation at 66 ± 4 d (see Fig. 10); however, as with *TESS*, WASP has a large pixel size (13.7 arcsec), and therefore the extraction aperture contains both TOI-6478 and its co-moving companion LP 789–76. Due to LP 789–76 being the brighter star, it is likely that this modulation does not come from TOI-6478. We therefore do not include this in our analysis but note that it prompts further observations of these stars from other ground-based observatories in order to untangle the origin of this signal.

[3] https://tess.mit.edu/followup

[4] https://exofop.ipac.caltech.edu/tess/target.php?id = 332657786

4.4 RV follow-up

4.4.1 MAROON-X

TOI-6478 was observed with the MAROON-X spectrograph at the Gemini North Observatory in Hilo, Hawai'i (Seifahrt et al. 2016, 2020, 2022). The MAROON-X spectrograph is a high-resolution RV spectrograph that uses red-optical fibre feeding and covers a wavelength range of 500–920 nm across two channels: blue (500–670 nm) and red (650–920 nm). It has a resolving power of $\sim$ 85 000.

We obtained 10 spectra with both the blue and red arms (645 and 875 nm, respectively) over a period of 27 d (2024 March 29 to 2024 April 23) with 900 s exposure time (see Table A1 in appendix). The mean SNR for the blue and red arms were 21 and 52, respectively. These data were reduced, with RVs extracted by the MAROON-X team using a specific version of the publicly available python pipeline SERVAL (SpEctrum Radial Velocity AnaLyser; Zechmeister et al. 2018), which has been modified for use with MAROON-X data, in which the analysis of the RVs is performed through a template matching code (see e.g. Winters et al. 2022; Kanodia et al. 2024; Martioli et al. 2024). This is favoured over other methods such as classical binary mask cross-correlation codes as it typically outperforms for M-dwarf stars. Correction for the main instrument drift is performed in the wavelength solution, and the Hα line is observed in both channels. It was noted that the 2024-04-01 09:22:47 (BJD 2460401.901) observation was flagged as 'usable' rather than 'pass', since the atmospheric dispersion compensator was not following the telescope. In order to be more conservative with our analyses (see Sections 5 and 6), we choose to omit this data point.

The cross-correlation function analysis confirmed the systemic velocity of TOI-6478 ($\sim 99.5\,\mathrm{km\,s^{-1}}$). We also measure the full width half-maximum (FWHM) of the average line profile, resulting in 5.4 ± 0.15 and $5.6 \pm 0.05\,\mathrm{km\,s^{-1}}$ for the blue and red channels, respectively. This corresponds to the expected FWHM of a non rotating M-dwarf at the resolution of MAROON-X. We can conclude that TOI-6478 is a slow rotating star with an upper limit of $v \sin i_\star \lesssim 2\,\mathrm{km\,s^{-1}}$.

4.5 Statistical validation

We make use of `TRICERATOPS`[5] (Giacalone & Dressing 2020; Giacalone et al. 2021), a statistical validation package used to evaluate the false positive probability (FPP) of TOI-6478 b.

Upon providing the *TESS* apertures for the target, `TRICERATOPS` calculates the amount of flux contributed from nearby stars, which enables it to assess whether the transit signal could be caused by an alternate scenario to that which is assumed, i.e. a transiting planet on the target star. Based on the aperture information, as well as the photometric data and high resolution speckle imaging constrast curves (Fig. 9), a range of scenarios for transiting planet and EBs are considered and their relative probabilities calculated. The threshold for a planet to be considered validated is FPP < 0.015.

Considering only the two transits from *TESS*, we find a FPP $=$ 0.6499 and a nearby false positive probability (NFPP) of NFPP $=$ 0.6498. This reduces to FPP $=$ NFPP $=$ 0.47 with the inclusion of the transit from LCO. We choose the light curve observed in the *i'* band for the validation since the transit depth, while statistically consistent between bands, is still wavelength-dependent (see Section 6), and the *TESS* bandpass is centred on *i'*. The FPP is rather large, likely due to the fact that our star is blended in the *TESS* aperture with its brighter comoving companion TIC 332657787 (LP 789-76 A), located $\sim$ 23 arcsec away. However, since the ground-based LCO data have a much smaller aperture situated only on the target star, the stars are resolved and we are able to confirm the transit is on target. Therefore, we adopt the procedure used in Timmermans et al. (2024)

[5] https://github.com/stevengiacalone/triceratops

Table 3. Fit parameters from global analysis of the photometry (see Section 5). The last column indicates whether the parameter was fixed for the nested sampler. The limb-darkening parameters for the two *TESS* transits are coupled.

Parameter	Value	Unit	Fit/fixed
	Fitted parameters		
$R_b/R_\star$	0.18027 ± 0.00088	$R_b/R_\star$	fit
$(R_\star + R_b)/a_b$	$0.01131^{+0.00011}_{-0.00013}$		fit
$\cos i_b$	$0.00178^{+0.00044}_{-0.00070}$		fit
$T_{0;b}$	$2459454.90101 \pm 0.00068$	BJD	fit
P_b	34.005019 ± 0.000025	d	fit
$\sqrt{e_b}\cos\omega_b$	0.0		fixed
$\sqrt{e_b}\sin\omega_b$	0.0		fixed
$D_{0;\mathrm{TESS\,S8}}$	0.182 ± 0.048		fit
$D_{0;\mathrm{TESS\,S62}}$	-0.125 ± 0.055		fit
$D_{0;\mathrm{LCO\,gp2m}}$	0.0		fixed
$D_{0;\mathrm{LCO\,ip2m}}$	0.0		fixed
$D_{0;\mathrm{LCO\,rp2m}}$	0.0		fixed
$D_{0;\mathrm{LCO\,zs2m}}$	0.0		fixed
$D_{0;\mathrm{LCO\,V1m}}$	0.0		fixed
$D_{0;\mathrm{LCO\,zs1m}}$	0.0		fixed
$q_{1;\mathrm{TESS\,S8}}$	0.256 ± 0.048		fit
$q_{2;\mathrm{TESS\,S8}}$	0.287 ± 0.049		fit
$q_{1;\mathrm{TESS\,S62}}$	0.2564481081075988		coupled
$q_{2;\mathrm{TESS\,S62}}$	0.2865715657990476		coupled
$q_{1;\mathrm{LCO\,gp2m}}$	0.732 ± 0.043		fit
$q_{2;\mathrm{LCO\,gp2m}}$	0.359 ± 0.037		fit
$q_{1;\mathrm{LCO\,ip2m}}$	$0.382^{+0.032}_{-0.030}$		fit
$q_{2;\mathrm{LCO\,ip2m}}$	$0.338^{+0.036}_{-0.033}$		fit
$q_{1;\mathrm{LCO\,rp2m}}$	0.641 ± 0.038		fit
$q_{2;\mathrm{LCO\,rp2m}}$	$0.378^{+0.032}_{-0.030}$		fit
$q_{1;\mathrm{LCO\,zs2m}}$	$0.279^{+0.030}_{-0.028}$		fit
$q_{2;\mathrm{LCO\,zs2m}}$	0.278 ± 0.039		fit
$q_{1;\mathrm{LCO\,V1m}}$	0.720 ± 0.045		fit
$q_{2;\mathrm{LCO\,V1m}}$	$0.345^{+0.042}_{-0.038}$		fit
$q_{1;\mathrm{LCO\,zs1m}}$	$0.254^{+0.041}_{-0.038}$		fit
$q_{2;\mathrm{LCO\,zs1m}}$	$0.275^{+0.049}_{-0.045}$		fit
$\ln\sigma_{\mathrm{TESS}}$	-4.560 ± 0.037		fit
$\ln\sigma_{\mathrm{TESS}}$	$-4.512^{+0.037}_{-0.035}$		fit
$\ln\sigma_{\mathrm{LCO}}$	-6.356 ± 0.093		fit
$\ln\sigma_{\mathrm{LCO}}$	$-6.181^{+0.027}_{-0.028}$		fit
$\ln\sigma_{\mathrm{LCO}}$	-6.396 ± 0.045		fit
$\ln\sigma_{\mathrm{LCO}}$	$-6.260^{+0.028}_{-0.026}$		fit
$\ln\sigma_{\mathrm{LCO}}$	$-5.989^{+0.089}_{-0.084}$		fit
$\ln\sigma_{\mathrm{LCO}}$	$-6.068^{+0.093}_{-0.088}$		fit

Table 4. Derived parameters for TOI-6478 b from global analysis of the photometry. All depths are fractional.

Parameter	Value	Source
Derived parameters		
Host radius over semimajor axis b; $R_\star/a_\mathrm{b}$	$0.009579^{+0.000088}_{-0.00010}$	derived
Semimajor axis b over host radius; $a_\mathrm{b}/R_\star$	$104.40^{+1.1}_{-0.95}$	derived
Companion radius b over semimajor axis b; $R_\mathrm{b}/a_\mathrm{b}$	$0.001727^{+0.000023}_{-0.000026}$	derived
Companion radius b; R_b ($\mathrm{R}_\oplus$)	4.60 ± 0.24	derived
Companion radius b; R_b (R_jup)	0.411 ± 0.021	derived
Semimajor axis b; a_b ($\mathrm{R}_\odot$)	24.4 ± 1.3	derived
Semimajor axis b; a_b (AU)	0.1136 ± 0.0060	derived
Inclination b; i_b (deg)	$89.898^{+0.040}_{-0.026}$	derived
Impact parameter b; $b_\mathrm{tra;b}$	$0.186^{+0.044}_{-0.072}$	derived
Total transit duration b; $T_\mathrm{tot;b}$ (h)	2.900 ± 0.011	derived
Full-transit duration b; $T_\mathrm{full;b}$ (h)	1.987 ± 0.015	derived
Host density from orbit b; $\rho_{\star;\mathrm{b}}$ (cgs)	$18.61^{+0.60}_{-0.50}$	derived
Equilibrium temperature b; $T_\mathrm{eq;b}$ (K)	204.4 ± 4.9	derived
Transit depth (undil.) b; $\delta_\mathrm{tr;undil;b;TESS\ S8}$	$0.0370^{+0.0031}_{-0.0029}$	derived
Transit depth (dil.) b; $\delta_\mathrm{tr;dil;b;TESS\ S8}$	$0.0303^{+0.0016}_{-0.0018}$	derived
Transit depth (undil.) b; $\delta_\mathrm{tr;undil;b;TESS\ S62}$	$0.0370^{+0.0025}_{-0.0023}$	derived
Transit depth (dil.) b; $\delta_\mathrm{tr;dil;b;TESS\ S62}$	$0.0416^{+0.0019}_{-0.0018}$	derived
Transit depth (undil.) b; $\delta_\mathrm{tr;undil;b;LCO\ gp2m}$	$0.04212^{+0.00056}_{-0.00052}$	derived
Transit depth (dil.) b; $\delta_\mathrm{tr;dil;b;LCO\ gp2m}$	$0.04212^{+0.00056}_{-0.00052}$	derived
Transit depth (undil.) b; $\delta_\mathrm{tr;undil;b;LCO\ ip2m}$	$0.03871^{+0.00029}_{-0.00033}$	derived
Transit depth (dil.) b; $\delta_\mathrm{tr;dil;b;LCO\ ip2m}$	$0.03871^{+0.00029}_{-0.00033}$	derived
Transit depth (undil.) b; $\delta_\mathrm{tr;undil;b;LCO\ rp2m}$	$0.04159^{+0.00037}_{-0.00034}$	derived
Transit depth (dil.) b; $\delta_\mathrm{tr;dil;b;LCO\ rp2m}$	$0.04159^{+0.00037}_{-0.00034}$	derived
Transit depth (undil.) b; $\delta_\mathrm{tr;undil;b;LCO\ zs2m}$	0.03722 ± 0.00029	derived
Transit depth (dil.) b; $\delta_\mathrm{tr;dil;b;LCO\ zs2m}$	0.03722 ± 0.00029	derived
Transit depth (undil.) b; $\delta_\mathrm{tr;undil;b;LCO\ V1m}$	0.04186 ± 0.00063	derived
Transit depth (dil.) b; $\delta_\mathrm{tr;dil;b;LCO\ V1m}$	0.04186 ± 0.00063	derived
Transit depth (undil.) b; $\delta_\mathrm{tr;undil;b;LCO\ zs1m}$	$0.03695^{+0.00054}_{-0.00050}$	derived
Transit depth (dil.) b; $\delta_\mathrm{tr;dil;b;LCO\ zs1m}$	$0.03695^{+0.00054}_{-0.00050}$	derived
Limb darkening; $u_\mathrm{1;TESS\ S8}$	$0.287^{+0.056}_{-0.052}$	derived
Limb darkening; $u_\mathrm{2;TESS\ S8}$	$0.213^{+0.058}_{-0.053}$	derived
Limb darkening; $u_\mathrm{1;LCO\ gp2m}$	0.614 ± 0.058	derived
Limb darkening; $u_\mathrm{2;LCO\ gp2m}$	0.240 ± 0.067	derived
Limb darkening; $u_\mathrm{1;LCO\ ip2m}$	0.418 ± 0.035	derived
Limb darkening; $u_\mathrm{2;LCO\ ip2m}$	0.200 ± 0.049	derived
Limb darkening; $u_\mathrm{1;LCO\ rp2m}$	0.606 ± 0.040	derived
Limb darkening; $u_\mathrm{2;LCO\ rp2m}$	0.195 ± 0.055	derived
Limb darkening; $u_\mathrm{1;LCO\ zs2m}$	$0.293^{+0.032}_{-0.034}$	derived
Limb darkening; $u_\mathrm{2;LCO\ zs2m}$	0.234 ± 0.050	derived
Limb darkening; $u_\mathrm{1;LCO\ V1m}$	0.586 ± 0.065	derived
Limb darkening; $u_\mathrm{2;LCO\ V1m}$	0.262 ± 0.072	derived
Limb darkening; $u_\mathrm{1;LCO\ zs1m}$	$0.276^{+0.050}_{-0.044}$	derived
Limb darkening; $u_\mathrm{2;LCO\ zs1m}$	0.226 ± 0.054	derived
Combined host density from all orbits; $\rho_{\star;\mathrm{combined}}$ (cgs)	$18.61^{+0.60}_{-0.50}$	derived

and remove the probability of a transiting planet around a nearby star, $P_{\rm NTP}$. This places the FPP at FPP $= 5.86 \times 10^{-18} \pm 7.045 \times 10^{-17}$, averaging from 20 iterations, which is well below the validated planet threshold.

5 GLOBAL ANALYSIS

We perform a global photometric analysis of both the *TESS* and LCO photometry using the flexible, publicly available PYTHON package ALLESFITTER (Günther & Daylan 2019, 2021). This inference-based package primarily makes use of the light curve generating PYTHON code ELLC (Maxted 2016), and the one-dimensional scalable Gaussian Process Regression code CELERITE (Foreman-Mackey et al. 2017). While both nested sampling (NS) and Markov Chain Monte Carlo algorithms can be used in ALLESFITTER [with the packages DYNESTY (Speagle 2020) and EMCEE (Foreman-Mackey et al. 2013), respectively] to obtain the best-fitting models, we select the NS method as this allows the Bayesian evidence to be calculated at each sampling step; this is particularly useful when wanting to compare different models, as from this we can calculate the Bayes factor (Kass & Raftery 1995) and assess which model, if any, is favoured. Since we initially run both circular and eccentric fits, this provides a quantitative argument as to which model should be assumed for this planetary system based on the data available.

We include all eight transits in our analysis of TOI-6478 b – 2×*TESS*, 6×LCO (same epoch) – however, we omit the RV data from our global fit. The *TESS* data used throughout this analysis are the SPOC Presearch Data Conditioning Simple Aperture Photometry (PDCSAP; Smith et al. 2012; Stumpe et al. 2012, 2014) 2-min *TESS* light curves (see Fig. 6). Once the global photometric fit is finalized, we use the results to do an RV-only fit, with tight priors on all parameters except semi-amplitude, K. This is discussed later in this section.

Initially we run two fits with both circular and eccentric models, where the eccentricity is either fixed at 0 or allowed to vary. Following Triaud et al. (2011), the eccentricity is reparametrized as $\sqrt{e_{\rm b}} \cos \omega_{\rm b}$ and $\sqrt{e_{\rm b}} \sin \omega_{\rm b}$, where $\omega_{\rm b}$ is the argument of periastron. We calculate the logarithm of the Bayes factor for the circular and eccentric cases to be 9964.3 and 9894.9, respectively. To significantly favour one scenario over another, it is often desired that $\Delta \log Z \geq 5$. We find $\Delta \log Z = 69.4$, therefore very clearly favouring the circular model over the eccentric. We use the stellar parameters described in Section 2 and uniformly fit for all planetary parameters, namely t_0, P, $\cos i$, $R_p/R_\star$, and $(R_p + R_\star)/a$.

Since the *TESS* apertures include a significant amount of light from stars other than the transit host (see Fig. 7), the observed transit depth needs to be corrected. Therefore, we fit for a dilution factor for the two *TESS* transits. This was the main motivation for fitting the *TESS* transits as separate instruments in ALLESFITTER, since it was likely they would have different dilution factors due to having different apertures. We fix the LCO dilution at 0 since there is no contamination due to the small aperture. As per the ALLESFITTER documentation, the dilution is equivalent to $D_0 = 1 - C$, where C is the 'crowdsap' value in the *TESS* FITS file headers. This gives the ratio of the the flux from the target star to the total flux within the aperture. For S8 and S62 we obtain $C_8 = 0.46$ and $C_{62} = 0.37$, respectively; however, we decide to freely fit the dilution with U[−1, 1] as this will also be informed by the uncontaminated LCO transits and we did not want to bias the fit if the crowdsap values are inaccurate.

For each photometric band, we calculate the quadratic limb-darkening coefficients using the PYTHON package PYLTDK (Parviainen & Aigrain 2015) and the PHOENIX stellar atmosphere library (Husser et al. 2013b). This code requires the $T_{\rm eff}$, log g, and metallicity, z, which are listed in Table 1. This gives us the u_1 and u_2 limb-darkening coefficients, which we reparametrize to q_1 and q_2 as in Kipping (2013). These are adopted as normal priors in our fit. We also make use of ALLESFITTER's 'coupled_with' function as for observations taken in the same photometric band we typically want the limb-darkening coefficients to agree. We apply this to the *TESS* light curves, but not to the two LCO transits taken in the z_s band in order to show that there is still agreement with the derived u_1 and u_2 values.

As expected, the light curves show variations from red noise caused by stellar variability and instrumental systematics; we choose to model the baseline with a hybrid spline for all data sets. While often a Gaussian process is used to account for this noise, this was not necessary since we model each transit separately, and hence there is no significant out-of-transit data. The hybrid spline works by automatically trying to describe the residuals with a smooth spline at every sampling step. This method does not require any parameters to be given as priors. We also use the 'error scaling' function within ALLESFITTER, which accounts for the white noise in our data; we give this a wide prior and select the 'sample' method, which samples as every other parameter.

We run a static NS within ALLESFITTER with 500 live points and a tolerance threshold of 0.02. We take the median posterior values as the results from our fit, with the uncertainty estimated as the 1σ confidence intervals. We then use these in an RV-only fit as mentioned above, again assuming a circular orbit. The results for the photometry-only and RV-only fits are shown in Figs 11 and 12, respectively. All fitted and derived parameters from the circular transit timing variation (TTV) fit are presented in Tables 3 and 4.

6 DISCUSSION AND CONCLUSION

From the circular fit using two transits from *TESS*, and six same-epoch transits from LCO, we find that TOI-6478 b hosts a ∼ Neptune-sized planet of radius $R_{\rm b} = 4.6 \pm 0.24\,{\rm R}_\oplus$ ($\sim 1.2\,{\rm R}_{\rm Nep}$) on a $P_{\rm b} = 34.005 \pm 0.000025$ d orbit.

We compare the stellar host density, $\rho_\star$, calculated from both orbital dynamics (i.e. a combination of the transit duration, impact parameter, and orbital period, assuming a circular orbit) and the stellar parameters (i.e. the mass and radius of the star); we find the derived stellar host density from our fit (which we do not use as a prior) to be $18.6^{+0.6}_{-0.5}$ g cm^{-3}, which is within 1.5σ of the prior value 25.27 ± 4.39 g cm^{-3}.

Fig. 13 shows the measured depths for each photometric band (corrected for limb darkening). These are obtained by doing a separate fit of the data where all bands have a uniform prior on the dilution factor (as for the *TESS* bands in Section 5) except one (i' here) as to act as a reference. This is to perform a chromaticity check on the measured depths across different wavelengths. We find that the transits are achromatic and agree to 1σ (except the bluest band g', which agrees to 1.3σ), which is indicative that the transiting events we observe are produced by a planet rather than a star in a binary orbit with TOI-6478 (or equally a nearby or background EB).

We note the potential presence of a star spot in the transits from LCO at around 2460373.06 BJD (see Fig. 11). We removed the spot and redid the analysis as described in Section 5 in order to test whether this was having an effect on the measured depth or duration of the transit. We find statistically consistent results to the original analysis and thus conclude this spot does not influence the fit. While

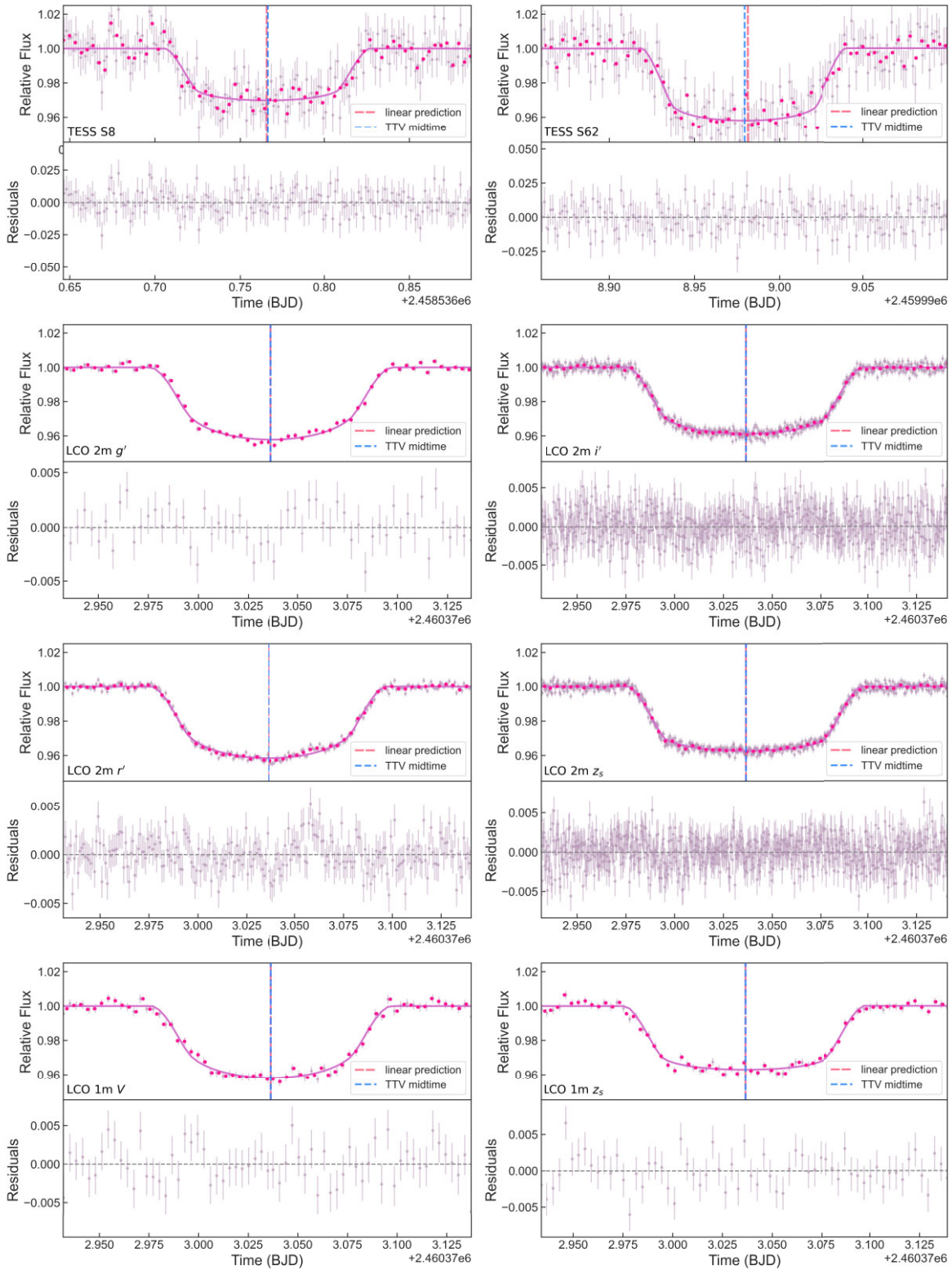

Figure 11. Fitted *TESS* (top two figures) and LCO transits (bottom six figures) obtained from the global photometric analysis using ALLESFITTER. The top panels show the model and transit data with the baseline subtracted, as well as the TTVs and linear predicted mid-time. The bottom panels show the residuals from our fit. The presence of a starspot is inferred from the LCO transits ($\sim$ 2460373.06 BJD).

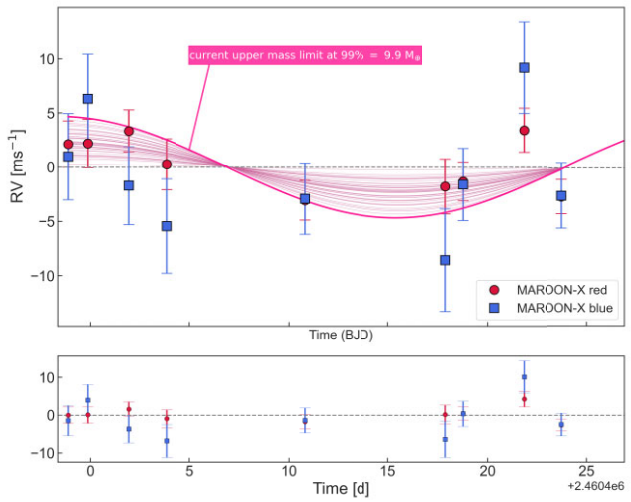

Figure 12. RV points measured with MAROON-X at the Gemini-North observatory. NS fit using both red- and blue-arm RV data achieved from results from global photometric analysis in order to obtain an upper limit on the semi-amplitude ($\leq 4.68\,\mathrm{m\,s^{-1}}$; bright pink line) and thus the mass of TOI-6478 b ($\leq 9.9\,\mathrm{M_\oplus}$). The darker pink lines show a sample of the posterior models from the fit. The bottom panel shows the residuals of the fit.

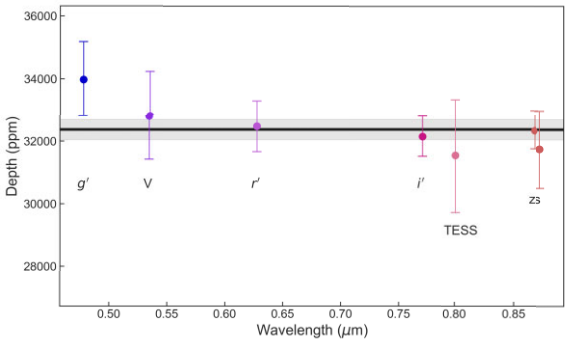

Figure 13. The measured transit depths for each transit versus wavelength, where for *TESS* this is the average from the two transits. The grey band shows the weighted average of the transit depths. All bands agree to 1σ except the blue band g', which agrees to 1.3σ.

the presence of a star spot presents an opportunity to measure spot properties on a late-type M-dwarf, it does have implications for the atmospheric characterization and mass measurements of the planet (see e.g. Boisse et al. 2011; Barstow et al. 2015; Vanderburg et al. 2016).

We fit the nine RVs (BJD = 2460401.901 data point omitted, see Section 4.4) with an NS using ALLESFITTER as discussed in Section 5 and from this calculate an upper limit on the semi-amplitude and thus an upper limit on the mass of the planet. We include both the red- and blue-arm RVs in this fit. From the mass–radius relations described in Chen & Kipping (2017), the estimated mass of a $4.6\,\mathrm{R_\oplus}$ planet is $19.2\,\mathrm{M_\oplus}$, which would produce an RV signal of $9.07\,\mathrm{m\,s^{-1}}$ assuming the orbital parameters from our fit. A signal of this amplitude is not seen in our RVs; instead we calculate the upper limit to be $K_{\mathrm{fit}} + 3\sigma$, where K_{fit} is the is semi-amplitude result from the NS and σ is the uncertainty on this measurement. From this we obtain $K_{\mathrm{max}} = 4.7\,\mathrm{m\,s^{-1}}$, which corresponds to a 3σ (99 per cent) upper mass limit of $m_{\mathrm{max}} = 9.9\,\mathrm{M_\oplus}$. Fig. 14(right) shows a mass–radius diagram for confirmed exoplanets (grey) along with key mass–radius relations (Zeng, Sasselov & Jacobsen 2016) (dashed lines) and Solar system planets (black). TOI-6478 b (pink) is placed at its current upper mass limit, where the pink arrow indicates the range of masses we expect to be its true mass. With decreasing mass, TOI-6478 b enters an underpopulated region of parameter space, which is of cold underdense Neptune-like exoplanets.

Fig. 15 shows all the TESS Objects of Interest (TOIs; Guerrero et al. 2021b) for stars with $T_{\mathrm{eff}} \leq 3300$ K (as of 2024 May 22). We remove non-planet entries (e.g. false positives, EBs, etc.) and calculate the equilibrium temperatures for each planet assuming an albedo of 0.3 (Earth). While we know this is likely not the albedo value for every planet, we adopt this here for consistency as this parameter is typically not available, especially for planet candidates. We find that TOI-6478 b is the coldest planet in the TOI sample for late-type M dwarfs. While there is one TOI planet candidate colder – TOI-5575.01,[6] an approximately Jupiter-sized object candidate orbiting a slightly cooler ($T_{\mathrm{eff}} = 3176 \pm 157$ K) star, we remove this from our Fig. 15 as observations have revealed that it is not a transiting exoplanet (Gan et al., in preparation).

The method discussed in Section 5 assumes a constant orbital period. In order to check from TTVs, we repeat same process but now allowing for TTVs in the fit. We use the uniform priors provided for the TTVs from ALLESFITTER, which have upper and lower bounds of $\mathrm{TTV_{mid}} \pm 0.01$ d (14.4 min). For this fit, we take the t_0 and P_{b} parameters from the linear fit (i.e. that discussed in Section 5) and fix them. TTVs typically occur if another body is present within the system, and have especially large amplitudes if the planets are in a mean motion resonance (see e.g. Rivera et al. 2010; Gillon et al. 2017; Lammers & Winn 2024). While the only available photometric data for TOI-6478 b consist of three transits, our fit does not show evidence of significant TTVs (see Fig. 16). Since there is significant time between the three transits (∼4 yr between transits 1 and 2, and ∼1 yr between transits 2 and 3), thus none are sequential, it is difficult to draw firm conclusions about whether there could be a second object in the system inducing TTVs.

6.1 Future observations

6.1.1 Constraining the mass with RVs

With nine RV data points from MAROON-X we were able to compute an upper limit to the mass of TOI-6478 b to be $M_b \leq 9.9\,\mathrm{M_\oplus}$. With the values from our fit, and assuming the orbit is circular, we can calculate the expected semi-amplitude for a given mass. We also attempt to estimate the smallest mass this planet could likely physically have, and find this value to be$4.5\,\mathrm{M_\oplus}$, based on the current known population of planets in this radius range; planets below $4.5\,\mathrm{M_\oplus}$ are typically rocky, whereas a planet of radius $4.6\,\mathrm{R_\oplus}$ is expected to be gaseous. This mass translates to a semi-amplitude signal of $2.12\,\mathrm{m\,s^{-1}}$. Knowing the uncertainty per measurement from MAROON-X to be $2.03\,\mathrm{m\,s^{-1}}$, we estimate a further 60 spectra are needed in order to confidently constrain the mass of TOI-6478 b.

6.1.2 JWST *atmospheric characterization*

TOI-6478 b represents a convenient opportunity to investigate cool, H_2-rich atmospheres. Its cold ($T_{\mathrm{eq}} = 204.4$ K) temperature is rivalled

[6] https://exofop.ipac.caltech.edu/tess/target.php?id = 160162137

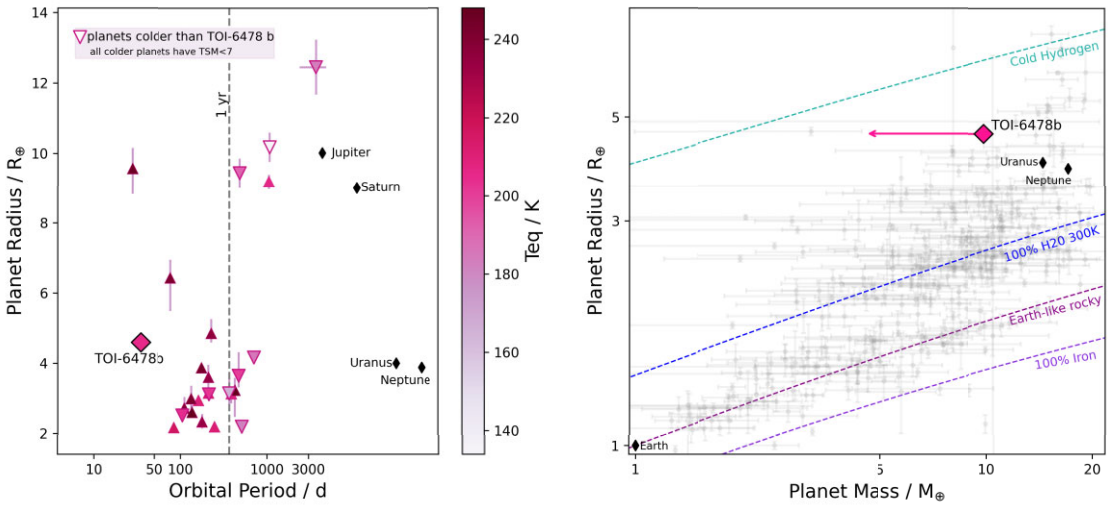

Figure 14. Comparison of TOI-6478 b (diamond) to the known exoplanet population. *Left*: planet radius versus orbital period for exoplanets with equilibrium temperatures (colour bar) < 250 K and radii $> 2\,R_\oplus$. One year is highlighted by the dashed grey line. Of these 25 exoplanets, only nine are colder than TOI-6478 b, but all have orbital periods at least $3\times$ larger. Solar systems planets are shown as reference. *Right*: mass–radius diagram with key mass–radius relations highlighted with coloured dashed lines. TOI-6478 b is shown as the pink diamond, placed at the upper mass limit from the current RVs. Solar system planets (black diamonds) are shown as reference.

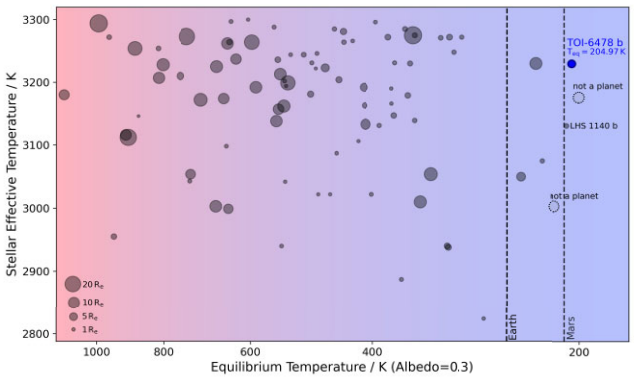

Figure 15. Effective temperature versus equilibrium temperature for all TOIs for $T_{\rm eff} \leq 3300$ K, with points as the relative sizes of the exoplanets. TOIs with non-planetary flags have been removed [False alarm (FA), false positive (FP), nearby eclipsing binary (NEB), background eclipsing binary (BEB), EB]. TOI-6478 b is highlighted in blue. Equilibrium temperatures for Earth and Mars are depicted by the dashed vertical lines. TOIs known not to be planetary in nature (TOI-6508 b, Barkaoui et al, in preparation; TOI-5575 b, Gan et al, in preparation), but have non-updated flags, have been included but highlighted as dashed circles. Well-known rocky super-Earth LHS 1140 b (Dittmann et al. 2017) is labelled. TOI-6478 b is the coldest TOI among late-type M dwarfs.

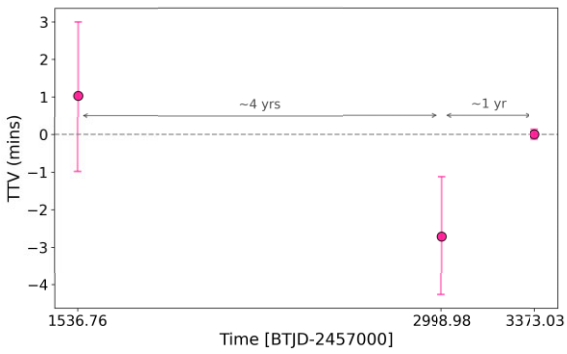

Figure 16. TTVs for TOI-6478 b from the global photometric analysis of the three transits (*TESS*×2, LCOGT×1 epoch), with approximate time between transits highlighted on the plot. No significant TTVs are detected. Nb: the error on the LCO transit TTV (third point) is small due to the fact that we fit six transits at this epoch (4x2m0, 2x1m0).

by only nine transiting planet[7] with radii $> 2\,R_\oplus$, see Fig. 14(left). However TOI-6478 b's orbital period is over $3\times$ shorter than the next coldest planet's, Kepler-309 c (Rowe et al. 2014), which has $P = 105.3$ d and $T_{\rm eq} = 204$ K. The majority of these planets with similar $T_{\rm eq}$ have $P > 1$ yr, posing obvious issues for detailed atmospheric characterization and follow-up observations, whereas TOI-6478 b transits almost monthly. Additionally, due to the underdense nature of the planet, its estimated minimum transmission spectroscopy metric (Kempton et al. 2018) is ~ 230 (based on the mass upper limit of $9.9\,M_\oplus$), which is significantly high compared to the other nine known colder transiting planet, which all have TSM < 7.[8]

We model the transmission spectrum of TOI-6478 b to demonstrate its observability (Fig. 17). The synthetic spectra are generated using the `Genesis` atmospheric model (Gandhi & Madhusudhan 2017; Piette & Madhusudhan 2020; Piette et al. 2023), coupled with the `FastChem Cond` equilibrium chemistry code (Stock et al. 2018; Kitzmann, Stock & Patzer 2024). We assume a $100\times$ solar elemental abundance, motivated by the metallicities of Neptune and

[7]Obtained from the composite NASA exoplanet archive (https://exoplanetarchive.ipac.caltech.edu/cgi-bin/TblView/nph-tblView?app=ExoTbls&config = PSCompPars) with the condition that planets must be transiting.

[8]The TSM is adapted for planets with $R_{\rm p} < 10\,R_\oplus$, and two of the cold planets have radii of $R_{\rm p} = 10.2\,R_\oplus$ and $R_{\rm p} = 12.44\,R_\oplus$. We use the scale factor for planets with $4.0 < R_{\rm p} < 10\,R_\oplus$ but note that these TSM values may not be fully comparable.

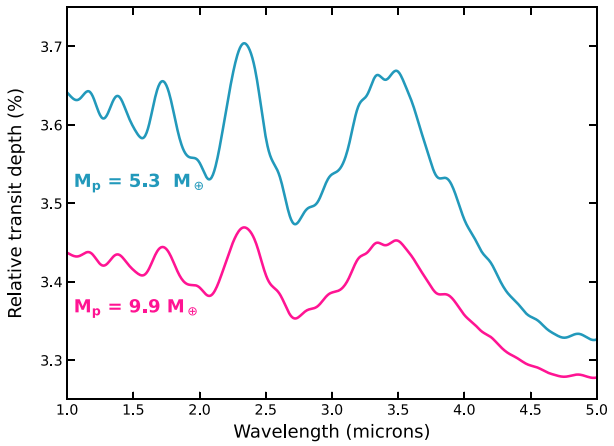

Figure 17. Model transmission spectra for TOI-6478 b corresponding to the upper mass limit (9.9 $M_\oplus$, pink) and the mass that results in a superpuff density of 0.3 g cm^{-3} (5.3 $M_\oplus$, blue). Both models assume a 100× solar atmospheric metallicity, and a simple aerosol prescription equivalent to 10^4 times H_2 Rayleigh scattering. The spectrum is dominated by CH_4 features at 1.4, 1.7, 2.3, and 3.3 μm.

Uranus' atmospheres (Atreya et al. 2018), and include the effects of rainout condensation. Given the ∼205 K temperature of this atmosphere, condensation is a key process and can significantly deplete the H_2O abundance in the upper atmosphere. The remaining atmospheric composition is dominated by H_2, He, and CH_4, with smaller contributions from NH_3. Given the prevalence of atmospheric clouds and hazes in Neptune-sized exoplanets (e.g. Brande et al. 2024), we include a simple aerosol prescription corresponding to H_2 Rayleigh scattering boosted by a factor of 10^4. Despite the high atmospheric metallicity and presence of aerosols, the near-infrared CH_4 features in these models are large, spanning several 100s ppm, even in the case of the upper mass limit.

ACKNOWLEDGEMENTS

The authors would like to acknowledge the MAROON-X team for their work on the reduction and analysis of the radial velocity data used in this work. Their thorough data analysis, clear communication, and willingness to assist with any inquiries have been greatly appreciated. We are grateful for their collaboration and support.

Funding for the *TESS* mission is provided by NASA's Science Mission Directorate. We acknowledge the use of public *TESS* data from pipelines at the TESS Science Office and at the TESS Science Processing Operations Center. KAC and CNW acknowledge support from the *TESS* mission via subaward s3449 from MIT.

This research has made use of the Exoplanet Follow-up Observation Program (ExoFOP; DOI: 10.26134/ExoFOP5) website, which is operated by the California Institute of Technology, under contract with the National Aeronautics and Space Administration under the Exoplanet Exploration Program.

This paper made use of data collected by the *TESS* mission and are publicly available from the Mikulski Archive for Space Telescopes (MAST) operated by the Space Telescope Science Institute (STScI). Resources supporting this work were provided by the NASA High-End Computing (HEC) Program through the NASA Advanced Supercomputing (NAS) Division at Ames Research Center for the production of the SPOC data products.

Some of the observations in this paper made use of the High-Resolution Imaging instrument Zorro and were obtained under Gemini LLP Proposal Number: GN/S-2021A-LP-105. Zorro was funded by the NASA Exoplanet Exploration Program and built at the NASA Ames Research Center by Steve B. Howell, Nic Scott, Elliott P. Horch, and Emmett Quigley. Zorro was mounted on the Gemini South telescope of the international Gemini Observatory, a program of NSF's OIR Lab, which is managed by the Association of Universities for Research in Astronomy (AURA) under a cooperative agreement with the National Science Foundation on behalf of the Gemini partnership: the National Science Foundation (United States), National Research Council (Canada), Agencia Nacional de Investigación y Desarrollo (Chile), Ministerio de Ciencia, Tecnología e Innovación (Argentina), Ministério da Ciência, Tecnologia, Inovações e Comunicações (Brazil), and Korea Astronomy and Space Science Institute (Republic of Korea).

This work makes use of observations from the LCOGT network. Part of the LCOGT telescope time was granted by NOIRLab through the Mid-Scale Innovations Program (MSIP). MSIP is funded by NSF.

This paper is based on observations made with the MuSCAT instruments, developed by the Astrobiology Center (ABC) in Japan, the University of Tokyo, and Las Cumbres Observatory (LCOGT). MuSCAT3 was developed with financial support by JSPS KAKENHI (JP18H05439) and JST PRESTO (JPMJPR1775), and is located at the Faulkes Telescope North on Maui, HI (USA), operated by LCOGT. MuSCAT4 was developed with financial support provided by the Heising-Simons Foundation (grant 2022–3611), JST grant number JPMJCR1761, and the ABC in Japan, and is located at the Faulkes Telescope South at Siding Spring Observatory (Australia), operated by LCOGT. This work is partly supported by JSPS KAKENHI Grant Number JP24H00017, JP24K00689 and JSPS Bilateral Program Number JPJSBP120249910.

The paper is based on observations made with the Kast spectrograph on the Shane 3m telescope at Lick Observatory. A major upgrade of the Kast spectrograph was made possible through generous gifts from the Heising-Simons Foundation as well as William and Marina Kast. We acknowledge that Lick Observatory sits on the unceded ancestral homelands of the Chochenyo and Tamyen Ohlone peoples, including the Alson and Socostac tribes, who were the original inhabitants of the area that includes Mt. Hamilton.

Visiting Astronomer at the Infrared Telescope Facility, which is operated by the University of Hawaii under contract 80HQTR24DA010 with the National Aeronautics and Space Administration.

This material is based upon work supported by the National Aeronautics and Space Administration under Agreement No. 80NSSC21K0593 for the program 'Alien Earths'. The results reported herein benefitted from collaborations and/or information exchange within NASA's Nexus for Exoplanet System Science (NExSS) research coordination network sponsored by NASA's Science Mission Directorate.

The postdoctoral fellowship of KB is funded by F.R.S.-FNRS grant T.0109.20 and by The Francqui Foundation.

This work was enabled by observations made from the Gemini North telescope, located within the Maunakea Science Reserve and adjacent to the summit of Maunakea. We are grateful for the privilege of observing the Universe from a place that is unique in both its astronomical quality and its cultural significance. Based on observations obtained at the international Gemini Observatory, a program of NSF NOIRLab, which is managed by the Association of Universities for Research in Astronomy (AURA) under a cooperative agreement with the U.S. National Science Foundation on behalf of the Gemini Observatory partnership: the U.S. National Science

Foundation (United States), National Research Council (Canada), Agencia Nacional de Investigación y Desarrollo (Chile), Ministerio de Ciencia, Tecnología e Innovación (Argentina), Ministério da Ciência, Tecnologia, Inovações e Comunicações (Brazil), and Korea Astronomy and Space Science Institute (Republic of Korea). Programme ID: GN-2024A-DD-102.

MGS acknowledges support from the UK Science and Technology Facilities Council (STFC).

DATA AVAILABILITY

TESS data products are available via the MAST portal at https://mast.stsci.edu/portal/Mashup/Clients/Mast/Portal.html.

REFERENCES

Atreya S. K., Crida A., Guillot T., Lunine J. I., Madhusudhan N., Mousis O., 2018, in Baines K. H., Flasar F. M., Krupp N., Stallard T.eds, Saturn in the 21st Century. p. 5
Bailer-Jones C. A. L., Rybizki J., Fouesneau M., Demleitner M., Andrae R., 2021, AJ, 161, 147
Baraffe I., Homeier D., Allard F., Chabrier G., 2015, A&A, 577, A42
Barkaoui K. et al., 2023, A&A, 677, A38
Barstow J. K., Aigrain S., Irwin P. G. J., Kendrew S., Fletcher L. N., 2015, MNRAS, 448, 2546
Benneke B. et al., 2019, ApJ, 887, L14
Bennett M., Bovy J., 2019, MNRAS, 482, 1417
Bensby T., Feltzing S., Lundström I., 2003, A&A, 410, 527
Bochanski J. J., West A. A., Hawley S. L., Covey K. R., 2007, AJ, 133, 531
Boisse I., Bouchy F., Hébrard G., Bonfils X., Santos N., Vauclair S., 2011, in Prasad Choudhary D., Strassmeier K. G.eds, Proc. IAU Symp. 273, Physics of Sun and Star Spots. Kluwer, Dordrecht, p. 281
Bovy J., 2015, ApJS, 216, 29
Brande J. et al., 2024, ApJ, 961, L23
Brown T. M. et al., 2013, PASP, 125, 1031
Burgasser A. J., Splat Development Team, 2017, in Coelho P., Martins L., Griffin E., eds, Astronomical Society of India Conference Series, Vol 14, The SpeX Prism Library Analysis Toolkit (SPLAT): A Data Curation Model, p. 7
Casagrande L., Flynn C., Bessell M., 2008, MNRAS, 389, 585
Chabrier G., 2003, PASP, 115, 763
Chen J., Kipping D., 2017, ApJ, 834, 17
Ciardi D. R., Beichman C. A., Horch E. P., Howell S. B., 2015, ApJ, 805, 16
Cochran W. D. et al., 2011, ApJS, 197, 7
Collins K., 2019, American Astronomical Society Meeting Abstracts #233. p. 140.05
Collins K. A., Kielkopf J. F., Stassun K. G., Hessman F. V., 2017, AJ, 153, 77
Cushing M. C., Vacca W. D., Rayner J. T., 2004, PASP, 116, 362
Cushing M. C., Rayner J. T., Vacca W. D., 2005, ApJ, 623, 1115
Cutri R. M. et al., 2003, VizieR Online Data Catalog, II/246
Cutri R. M. et al., 2021, VizieR Online Data Catalog, II/328
Davis Y. T. et al., 2024, MNRAS, 530, 2565
Delrez L. et al., 2022, A&A, 667, A59
Dittmann J. A. et al., 2017, Nature, 544, 333
Duck A. et al., 2023, MNRAS, 521, 6305
Eisner N. L. et al., 2021, MNRAS, 501, 4669
Foreman-Mackey D., Hogg D. W., Lang D., Goodman J., 2013, PASP, 125, 306
Foreman-Mackey D., Agol E., Ambikasaran S., Angus R., 2017, Astrophysics Source Code Library, record ascl:1709.008
Furlan E., Howell S. B., 2017, AJ, 154, 66
Furlan E., Howell S. B., 2020, ApJ, 898, 47
Gaia Collaboration, 2022, VizieR Online Data Catalog, I/355
Gaia Collaboration, 2016, A&A, 595, A1
Gaia Collaboration, 2021, A&A, 649, A6
Gaia Collaboration, 2023, A&A, 674, A1
Gandhi S., Madhusudhan N., 2017, MNRAS, 472, 2334
Gao P., Zhang X., 2020, ApJ, 890, 93
Ghachoui M. et al., 2023, A&A, 677, A31
Giacalone S., Dressing C. D., 2020, Astrophysics Source Code Library, record ascl:2002.004
Giacalone S. et al., 2021, AJ, 161, 24
Gillon M. et al., 2017, Nature, 542, 456
Gillon M. et al., 2024, Nat. Astron., 8, 865
Gravity Collaboration, 2019, A&A, 625, L10
Guerrero N. M. et al., 2021a, ApJS, 254, 39
Guerrero N. M. et al., 2021b, ApJS, 254, 39
Günther M. N., Daylan T., 2019, Astrophysics Source Code Library, record ascl:1903.003
Günther M. N., Daylan T., 2021, ApJS, 254, 13
Hallatt T., Lee E. J., 2025, ApJ, 979, 120
Hardegree-Ullman K. K., Apai D., Bergsten G. J., Pascucci I., López-Morales M., 2023, AJ, 165, 267
Henry T. J., Jao W.-C., Subasavage J. P., Beaulieu T. D., Ianna P. A., Costa E., Méndez R. A., 2006, AJ, 132, 2360
Howell S. B., Everett M. E., Sherry W., Horch E., Ciardi D. R., 2011, AJ, 142, 19
Howell S. B., Everett M. E., Horch E. P., Winters J. G., Hirsch L., Nusdeo D., Scott N. J., 2016, ApJ, 829, L2
Huang C. X. et al., 2020a, Res. Notes Am. Astron. Soc., 4, 204
Huang C. X. et al., 2020b, Res. Notes Am. Astron. Soc., 4, 206
Husser T. O., Wende-von Berg S., Dreizler S., Homeier D., Reiners A., Barman T., Hauschildt P. H., 2013a, A&A, 553, A6
Husser T. O., Wende-von Berg S., Dreizler S., Homeier D., Reiners A., Barman T., Hauschildt P. H., 2013b, A&A, 553, A6
Jenkins J. M., 2002, ApJ, 575, 493
Jenkins J. M. et al., 2010, in Radziwill N. M., Bridger A.eds, Proc. SPIE Conf. Ser. Vol. 7740, Software and Cyberinfrastructure for Astronomy. SPIE, Bellingham, p. 77400D
Jenkins J. M. et al., 2016, in Chiozzi G., Guzman J. C.eds, Proc. SPIE Conf. Ser. Vol. 9913, Software and Cyberinfrastructure for Astronomy IV. SPIE, Bellingham, p. 99133E
Jenkins J. M., Tenenbaum P., Seader S., Burke C. J., McCauliff S. D., Smith J. C., Twicken J. D., Chandrasekaran H., 2020, Kepler Data Processing Handbook: Transiting Planet Search, Kepler Science Document KSCI-19081-003
Jensen E., 2013, Astrophysics Source Code Library, record ascl:1306.007
Kanodia S. et al., 2024, AJ, 168, 235
Kass R. E., Raftery A. E., 1995, J. Am. Stat. Assoc., 90, 773
Kempton E. M. R. et al., 2018, PASP, 130, 114401
Kempton E. M. R. et al., 2023, Nature, 620, 67
Kesseli A. Y., Muirhead P. S., Mann A. W., Mace G., 2018, AJ, 155, 225
Kipping D. M., 2013, MNRAS, 435, 2152
Kitzmann D., Stock J. W., Patzer A. B. C., 2024, MNRAS, 527, 7263
Kunimoto M., Daylan T., 2021, in Posters from the TESS Science Conference II (TSC2). p. 62
Lammers C., Winn J. N., 2024, ApJ, 968, L12
Lasker B. M., Doggett J., McLean B., Sturch C., Djorgovski S., de Carvalho R. R., Reid I. N., 1996, in Jacoby G. H., Barnes J.eds, ASP Conf. Ser. Vol. 101, Astronomical Data Analysis Software and Systems V. Astron. Soc. Pac., San Francisco, p. 88
Lépine S., Rich R. M., Shara M. M., 2003, AJ, 125, 1598
Lépine S., Rich R. M., Shara M. M., 2007, ApJ, 669, 1235
Lépine S., Hilton E. J., Mann A. W., Wilde M., Rojas-Ayala B., Cruz K. L., Gaidos E., 2013, AJ, 145, 102
Lester K. V. et al., 2021, AJ, 162, 75
Li J., Tenenbaum P., Twicken J. D., Burke C. J., Jenkins J. M., Quintana E. V., Rowe J. F., Seader S. E., 2019, PASP, 131, 024506

Madhusudhan N., Nixon M. C., Welbanks L., Piette A. A. A., Booth R. A., 2020, ApJ, 891, L7
Mann A. W., Brewer J. M., Gaidos E., Lépine S., Hilton E. J., 2013, AJ, 145, 52
Mann A. W., Feiden G. A., Gaidos E., Boyajian T., von Braun K., 2016, ApJ, 819, 87
Martioli E. et al., 2024, A&A, 690, A312
Massey P., Gronwall C., 1990, ApJ, 358, 344
Maxted P. F. L., 2016, A&A, 591, A111
Maxted P. F. L., Triaud A. H. M. J., Martin D. V., 2023, Universe, 9, 498
McCully C., Volgenau N. H., Harbeck D.-R., Lister T. A., Saunders E. S., Turner M. L., Siiverd R. J., Bowman M., 2018, in Guzman J. C., Ibsen J., eds, Proc. SPIE Conf. Ser. Vol. 10707, Software and Cyberinfrastructure for Astronomy V. SPIE, Bellingham, p. 107070K
McMillan P. J., 2017, MNRAS, 465, 76
Miller J. S., Stone R. P. S., 1994, Technical Report66, The Kast Double Spectrograph. University of California Lick Observatory Technical Reports
Moya A., Zuccarino F., Chaplin W. J., Davies G. R., 2018, ApJS, 237, 21
Narita N. et al., 2020, in Evans C. J., Bryant J. J., Motohara K., eds, Proc. SPIE Conf. Ser. Vol. 11447, Ground-based and Airborne Instrumentation for Astronomy VIII. SPIE, Bellingham, p. 114475K
Nettelmann N., Kramm U., Redmer R., Neuhäuser R., 2010, A&A, 523, A26
Oke J. B., 1990, AJ, 99, 1621
Parviainen H., Aigrain S., 2015, MNRAS, 453, 3821
Pecaut M. J., Mamajek E. E., 2013, ApJS, 208, 9
Pickles A. J., 1998, PASP, 110, 863
Piette A. A. A., Madhusudhan N., 2020, ApJ, 904, 154
Piette A. A. A., Gao P., Brugman K., Shahar A., Lichtenberg T., Miozzi F., Driscoll P., 2023, ApJ, 954, 29
Piro A. L., Vissapragada S., 2020, AJ, 159, 131
Pollacco D. L. et al., 2006, PASP, 118, 1407
Rayner J. T., Toomey D. W., Onaka P. M., Denault A. J., Stahlberger W. E., Vacca W. D., Cushing M. C., Wang S., 2003, PASP, 115, 362
Rayner J. T., Cushing M. C., Vacca W. D., 2009, ApJS, 185, 289
Rebassa-Mansergas A. et al., 2023, MNRAS, 526, 4787
Reefe M. A. et al., 2022, AJ, 163, 269
Reid I. N. et al., 1991, PASP, 103, 661
Reylé C., Jardine K., Fouqué P., Caballero J. A., Smart R. L., Sozzetti A., 2021, A&A, 650, A201
Ricker G. R. et al., 2015, J. Astron. Telesc. Instrum. Syst., 1, 014003
Rivera E. J., Laughlin G., Butler R. P., Vogt S. S., Haghighipour N., Meschiari S., 2010, ApJ, 719, 890
Rojas-Ayala B., Covey K. R., Muirhead P. S., Lloyd J. P., 2012, ApJ, 748, 93
Rowe J. F. et al., 2014, ApJ, 784, 45
Santerne A. et al., 2019, preprint (arXiv:1911.07355)
Schönrich R., Binney J., Dehnen W., 2010, MNRAS, 403, 1829
Scott N. J. et al., 2021, Front. Astron. Space Sci., 8, 138
Seager S., Deming D., 2010, ARA&A, 48, 631
Sebastian D. et al., 2021, A&A, 645, A100
Seifahrt A., Bean J. L., Stürmer J., Gers L., Grobler D. S., Reed T., Jones D. J., 2016, in Evans C. J., Simard L., Takami H.eds, Proc. SPIE Conf. Ser. Vol. 9908, Ground-based and Airborne Instrumentation for Astronomy VI. SPIE, Bellingham, p. 990818
Seifahrt A. et al., 2020, in Evans C. J., Bryant J. J., Motohara K.eds, Proc. SPIE Conf. Ser. Vol. 11447, Ground-based and Airborne Instrumentation for Astronomy VIII. SPIE, Bellingham, p. 114471F
Seifahrt A. et al., 2022, in Evans C. J., Bryant J. J., Motohara K.eds, Proc. SPIE Conf. Ser. Vol. 12184, Ground-based and Airborne Instrumentation for Astronomy IX. SPIE, Bellingham, p. 121841G
Smith J. C. et al., 2012, PASP, 124, 1000
Spada F., Demarque P., Kim Y. C., Sills A., 2013, ApJ, 776, 87
Speagle J. S., 2020, MNRAS, 493, 3132
Spitoni E., Matteucci F., Gratton R., Ratcliffe B., Minchev I., Cescutti G., 2024, A&A, 690, A208
Stassun K. G., Torres G., 2016, AJ, 152, 180
Stassun K. G., Torres G., 2021, ApJ, 907, L33
Stassun K. G., Collins K. A., Gaudi B. S., 2017, AJ, 153, 136
Stassun K. G., Corsaro E., Pepper J. A., Gaudi B. S., 2018, AJ, 155, 22
Stassun K. G. et al., 2019, AJ, 158, 138
Stock J. W., Kitzmann D., Patzer A. B. C., Sedlmayr E., 2018, MNRAS, 479, 865
Stumpe M. C. et al., 2012, PASP, 124, 985
Stumpe M. C., Smith J. C., Catanzarite J. H., Van Cleve J. E., Jenkins J. M., Twicken J. D., Girouard F. R., 2014, PASP, 126, 100
Swayne M. I. et al., 2024, MNRAS, 528, 5703
The JWST Transiting Exoplanet Community Early Release Science Team, 2022, Nature, 7949, 649
Timmermans M. et al., 2024, A&A, 687, A48
Torres G., Andersen J., Giménez A., 2010, A&AR, 18, 67
Triaud A. H. M. J., 2021, in Madhusudhan N.ed., ExoFrontiers; Big Questions in Exoplanetary Science. IOP Publishing, Bristol, p. 6
Triaud A. H. M. J. et al., 2011, A&A, 531, A24
Triaud A. H. M. J. et al., 2013, A&A, 549, A18
Triaud A. H. M. J. et al., 2023, MNRAS, 525, L98
Twicken J. D. et al., 2018, PASP, 130, 064502
Vanderburg A., Plavchan P., Johnson J. A., Ciardi D. R., Swift J., Kane S. R., 2016, MNRAS, 459, 3565
Weeks A. et al., 2025, MNRAS, 539, 405
West A. A., Hawley S. L., Bochanski J. J., Covey K. R., Reid I. N., Dhital S., Hilton E. J., Masuda M., 2008, AJ, 135, 785
Winters J. G. et al., 2022, AJ, 163, 168
Zechmeister M. et al., 2018, A&A, 609, A12
Zeng L., Sasselov D. D., Jacobsen S. B., 2016, ApJ, 819, 127
Zink J. K. et al., 2023, AJ, 165, 262

APPENDIX A: RV DATA

In Table A1 we provide the 10 RV data points obtained with the MAROON-X spectrograph in Hawai'i.

Table A1. MAROON-X observations of TOI-6478, where the red and blue columns denote the red and blue arms of the spectrograph, respectively.

BJD (d)	Red			Blue		
	RV ($m\,s^{-1}$)	σ ($m\,s^{-1}$)	SNR	RV ($m\,s^{-1}$)	σ ($m\,s^{-1}$)	SNR
2460398.89216	2.12	2.15	50.0	0.96	3.99	20.0
2460399.87039	2.18	2.23	48.0	6.31	4.13	19.0
2460401.90117[a]	−1.35	2.00	54.0	−6.15	4.66	19.0
2460401.91435	3.34	1.94	54.0	−1.72	3.59	22.0
2460403.81640	0.26	2.34	46.0	−5.44	4.34	18.0
2460410.81273	−3.06	1.82	58.0	−2.92	3.28	24.0
2460417.88471	−1.79	2.53	41.0	−8.56	4.73	17.0
2460418.77670	−1.33	1.78	56.0	−1.61	3.33	23.0
2460421.83060	3.39	2.04	49.0	9.18	4.22	19.0
2460423.74191	−2.68	1.60	61.0	−2.60	3.00	25.0

Note.[a]This data point is omitted from our analysis as it was flagged as 'usable' rather than 'pass', and we wanted to remain conservative when obtaining an upper mass limit.

[1]*School of Physics and Astronomy, University of Birmingham, Edgbaston, Birmingham B15 2TT, UK*
[2]*Astrobiology Research Unit, University of Liège, Allée du 6 août, 19, B-4000 Liège (Sart-Tilman), Belgium*
[3]*Department of Earth, Atmospheric and Planetary Sciences, MIT, 77 Massachusetts Avenue, Cambridge, MA 02139, USA*
[4]*Instituto de Astrofísica de Canarias (IAC), Calle Vía Láctea s/n, E-38200 La Laguna, Tenerife, Spain*
[5]*Department of Astronomy & Astrophysics, UC San Diego, 9500 Gilman Drive, La Jolla, CA 92093, USA*
[6]*Center for Astrophysics | Harvard & Smithsonian, 60 Garden Street, Cambridge, MA 02138, USA*
[7]*Department of Astrophysics, University of Oxford, Denys Wilkinson Building, Keble Road, Oxford OX1 3RH, UK*
[8]*Magdalen College, University of Oxford, Oxford OX1 4AU, UK*
[9]*Astrophysics Group, Keele University, Staffordshire ST5 5BG, UK*
[10]*NASA Ames Research Center, Moffett Field, CA 94035, USA*
[11]*Department of Physics and Astronomy, Vanderbilt University, 6301 Stevenson Center Lane, Nashville, TN 37235, USA*
[12]*Department of Physics and Astronomy, Texas Tech University, Lubbock TX, 79409-1051, USA*
[13]*Komaba Institute for Science, The University of Tokyo, 3-8-1 Komaba, Meguro, Tokyo 153-8902, Japan*
[14]*Astrobiology Center, 2-21-1 Osawa, Mitaka, Tokyo 181-8588, Japan*
[15]*Kavli Institute for Astrophysics and Space Research, Massachusetts Institute of Technology, Cambridge, MA 02139, USA*
[16]*Departamento de Astrofísica, Universidad de La Laguna (ULL), E-38206 La Laguna, Tenerife, Spain*
[17]*Department of Astronomy, University of Maryland, College Park, MD 20742, USA*
[18]*Department of Physics and Kavli Institute for Astrophysics and Space Research, Massachusetts Institute of Technology, Cambridge, MA 02139, USA*
[19]*SETI Institute, Mountain View, CA 94043 USA*
[20]*Department of Astrophysical Sciences, Princeton University, Princeton, NJ 08544, USA*
[21]*Planetary Discoveries, Valencia, CA 91354, USA*

This paper has been typeset from a TEX/LATEX file prepared by the author.